Article

Cell Metabolism

Quiescent Endothelial Cells Upregulate Fatty Acid β-Oxidation for Vasculoprotection via Redox Homeostasis

Graphical Abstract

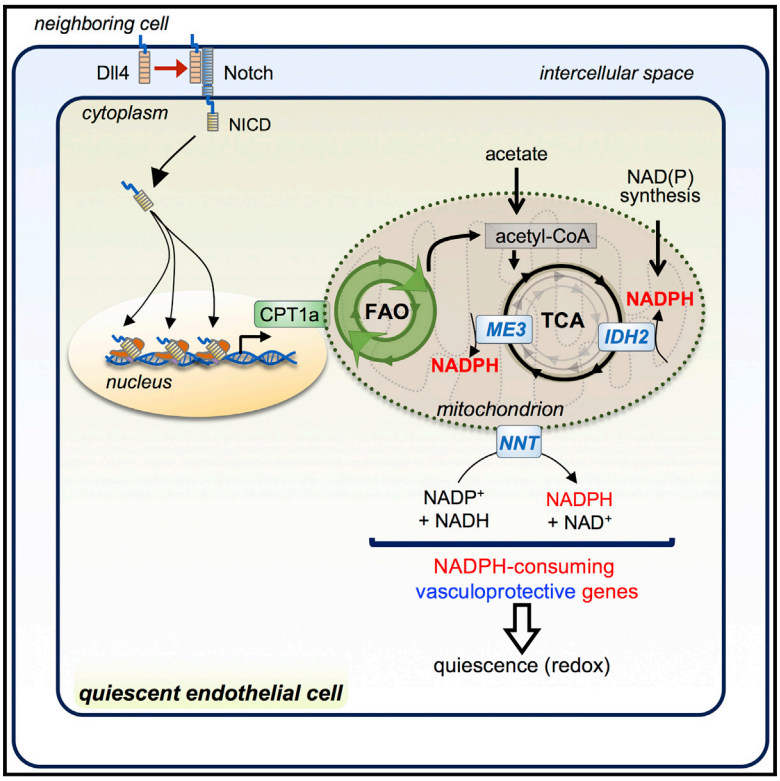

Authors

Joanna Kalucka, Laura Bierhansl, Nadine Vasconcelos Conchinha, ..., Xuri Li, Sarah-Maria Fendt, Peter Carmeliet

Correspondence

lixr6@mail.sysu.edu.cn (X.L.), peter.carmeliet@kuleuven.vib.be (P.C.)

In Brief

Kalucka et al. show that fatty acid β-oxidation in quiescent endothelial cells (QECs) is indispensable to maintain redox balance and prevent EC dysfunction. In contrast to proliferating ECs (PECs), QECs reprogram their metabolism to increase regeneration of NAPDH, which is then used by vasculoprotective (NADPH-consuming) enzymes for redox homeostasis.

Highlights

- QECs reprogram their metabolism to enhance redox homeostasis
- QECs rely on fatty acid β-oxidation (FAO) to increase NADPH regeneration
- Inhibition of FAO in QECs results in QEC dysfunction, which is rescued by acetate
- Notch signaling upregulates transcription of CPT1A, a rate-controlling step in FAO

Data Resources

GSE89174
E-MTAB-6595

Kalucka et al., 2018, Cell Metabolism *28*, 881–894
December 4, 2018
https://doi.org/10.1016/j.cmet.2018.07.016

CellPress

Cell Metabolism
Article

Quiescent Endothelial Cells Upregulate Fatty Acid β-Oxidation for Vasculoprotection via Redox Homeostasis

Joanna Kalucka,[1,2,3,19] Laura Bierhansl,[1,3,19] Nadine Vasconcelos Conchinha,[1,3,19] Rindert Missiaen,[1,3,19] Ilaria Elia,[4,5] Ulrike Brüning,[1,3] Samantha Scheinok,[6] Lucas Treps,[1,3] Anna Rita Cantelmo,[1,3] Charlotte Dubois,[1,3] Pauline de Zeeuw,[1,3] Jermaine Goveia,[1,3] Annalisa Zecchin,[1,3] Federico Taverna,[1,3] Francisco Morales-Rodriguez,[1,3] Aleksandra Brajic,[1,3] Lena-Christin Conradi,[1,3] Sandra Schoors,[1,3] Ulrike Harjes,[1,3] Kim Vriens,[4,5] Gregor-Alexander Pilz,[7] Rongyuan Chen,[2] Richard Cubbon,[8] Bernard Thienpont,[9,10] Bert Cruys,[1,3] Brian W. Wong,[1,3] Bart Ghesquière,[11,12] Mieke Dewerchin,[1,3] Katrien De Bock,[1,3,18] Xavier Sagaert,[13] Sebastian Jessberger,[7] Elizabeth A.V. Jones,[14,15] Bernard Gallez,[6] Diether Lambrechts,[9,10] Massimiliano Mazzone,[16,17] Guy Eelen,[1,3] Xuri Li,[2,*] Sarah-Maria Fendt,[4,5] and Peter Carmeliet[1,2,3,20,*]

[1]Laboratory of Angiogenesis and Vascular Metabolism, VIB Center for Cancer Biology (CCB), VIB, 3000 Leuven, Belgium
[2]State Key Laboratory of Ophthalmology, Zhongshan Ophthalmic Center, Sun Yat-Sen University, Guangzhou 51006, Guangdong, P.R. China
[3]Laboratory of Angiogenesis and Vascular Metabolism, Department of Oncology and Leuven Cancer Institute (LKI), KU Leuven, 3000 Leuven, Belgium
[4]Laboratory of Cellular Metabolism and Metabolic Regulation, Department of Oncology and Leuven Cancer Institute (LKI), KU Leuven, 3000 Leuven, Belgium
[5]Laboratory of Cellular Metabolism and Metabolic Regulation, VIB Center for Cancer Biology, Center for Cancer Biology (CCB), VIB, 3000 Leuven, Belgium
[6]Université Catholique de Louvain, Louvain Drug Research Institute, Biomedical Magnetic Resonance Research Group, 1200 Brussels, Belgium
[7]Brain Research Institute, Faculty of Medicine and Science, University of Zurich, Zurich 8057, Switzerland
[8]Division of Cardiovascular and Diabetes Research, Multidisciplinary Cardiovascular Research Centre, University of Leeds, Leeds LS2 9JT, UK
[9]Laboratory of Translational Genetics, Department of Oncology and Leuven Cancer Institute (LKI), KU Leuven, 3000 Leuven, Belgium
[10]Laboratory of Translational Genetics, VIB Center for Cancer Biology (CCB), VIB, 3000 Leuven, Belgium
[11]Metabolomics Expertise Center, VIB Center for Cancer Biology (CCB), VIB, 3000 Leuven, Belgium
[12]Metabolomics Expertise Center, Department of Oncology, KU Leuven, 3000 Leuven, Belgium
[13]Translational Cell & Tissue Research, Department of Imaging & Pathology, KU Leuven, 3000 Leuven, Belgium
[14]Department of Cardiovascular Sciences, KU Leuven, UZ Herestraat 49, Box 911, 3000 Leuven, Belgium
[15]Centre for Molecular and Vascular Biology, KU Leuven, UZ Herestraat 49, Box 911, 3000 Leuven, Belgium
[16]Laboratory of Tumor Inflammation and Angiogenesis, VIB Center for Cancer Biology (CCB), VIB, 3000 Leuven, Belgium
[17]Laboratory of Tumor Inflammation and Angiogenesis, Department of Oncology, University of Leuven, 3000 Leuven, Belgium
[18]Present address: Laboratory of Exercise and Health, Department of Health Sciences and Technology, Swiss Federal Institute of Technology (ETH) Zurich, Schwerzenbach 8603, Switzerland
[19]These authors contributed equally
[20]Lead Contact
*Correspondence: lixr6@mail.sysu.edu.cn (X.L.), peter.carmeliet@kuleuven.vib.be (P.C.)
https://doi.org/10.1016/j.cmet.2018.07.016

SUMMARY

Little is known about the metabolism of quiescent endothelial cells (QECs). Nonetheless, when dysfunctional, QECs contribute to multiple diseases. Previously, we demonstrated that proliferating endothelial cells (PECs) use fatty acid β-oxidation (FAO) for *de novo* dNTP synthesis. We report now that QECs are not hypometabolic, but upregulate FAO >3-fold higher than PECs, not to support biomass or energy production but to sustain the tricarboxylic acid cycle for redox homeostasis through NADPH regeneration. Hence, endothelial loss of FAO-controlling CPT1A in CPT1A$^{\Delta EC}$ mice promotes EC dysfunction (leukocyte infiltration, barrier disruption) by increasing endothelial oxidative stress, rendering CPT1A$^{\Delta EC}$ mice more susceptible to LPS and inflammatory bowel disease. Mechanistically, Notch1 orchestrates the use of FAO for redox balance in QECs. Supplementation of acetate (metabolized to acetyl-coenzyme A) restores endothelial quiescence and counters oxidative stress-mediated EC dysfunction in CPT1A$^{\Delta EC}$ mice, offering therapeutic opportunities. Thus, QECs use FAO for vasculoprotection against oxidative stress-prone exposure.

INTRODUCTION

Dysfunctional endothelial cells (ECs) contribute to numerous diseases with high morbidity and mortality, including atherosclerosis, stroke, diabetes, and glaucoma, affecting millions of people

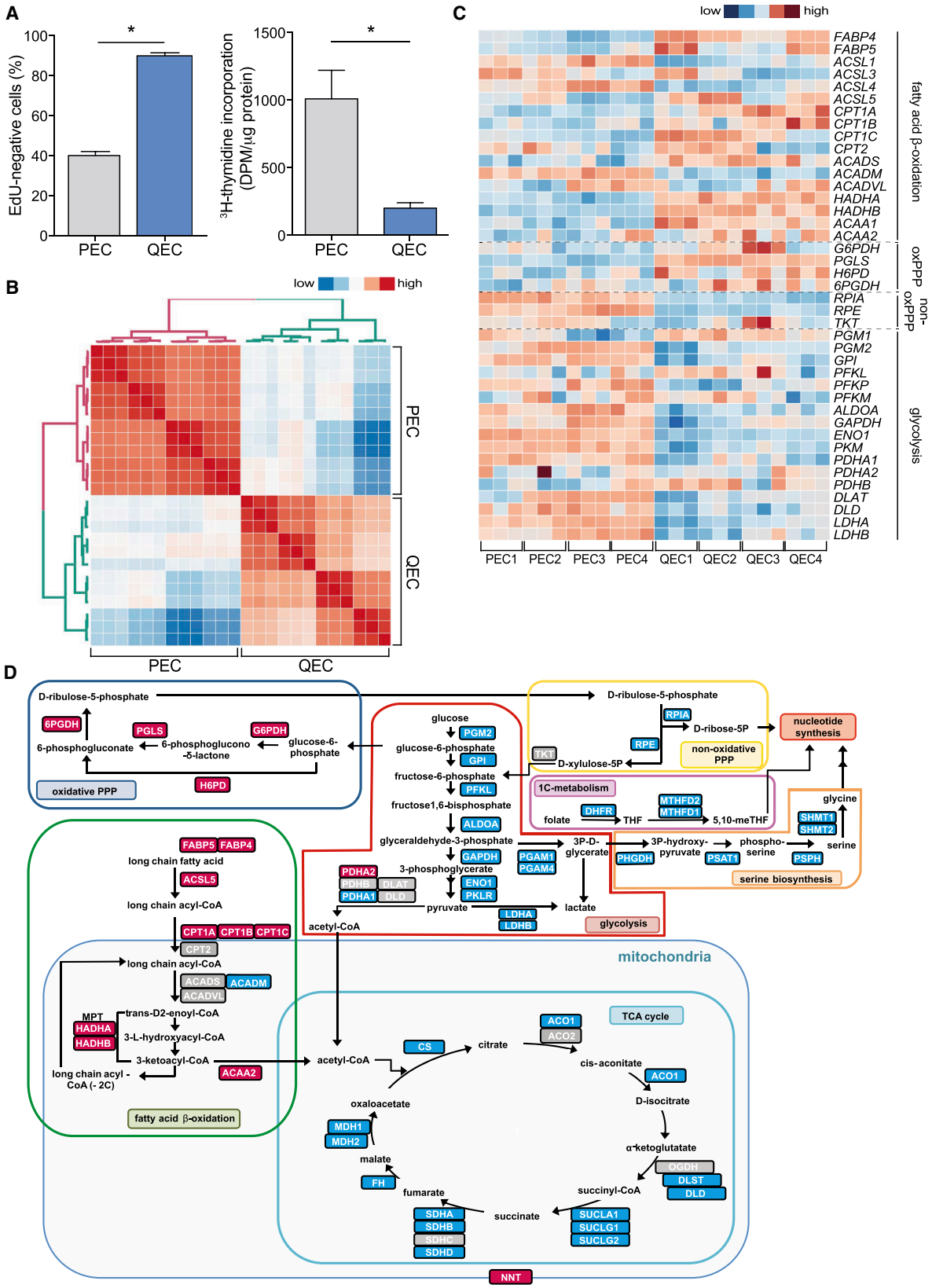

(legend on next page)

worldwide. Hence, reversal or prevention of EC dysfunction is a therapeutic objective, and understanding how quiescent endothelial cells (QECs) protect themselves against dysfunction is an unmet medical need. Most ECs in a healthy adult are quiescent (Eelen et al., 2018). They mediate tissue perfusion, counteract thrombosis and vascular inflammation, and maintain vasoregulation and barrier function (Chistiakov et al., 2017; Incalza et al., 2018). QECs are, however, exposed to high oxygen levels, and thus prone to oxidative stress (Polet and Feron, 2013), known to induce EC dysfunction in multiple cardiovascular disorders (Chistiakov et al., 2017). We hypothesized that QECs must therefore possess metabolic mechanisms to protect themselves against oxidative stress. However, a possible involvement of cellular metabolism in EC quiescence has not been considered, and it is unknown whether metabolic changes accompany or underlie the vasculoprotective homeostatic phenotype of QECs.

Nonetheless, a role for EC metabolism is suggested. Indeed, (1) EC dysfunction can result from enhanced oxidative stress, generated by uncoupled endothelial nitric oxide synthase (eNOS) and mitochondrial respiration (Eelen et al., 2018). (2) Pathways sensing changes in cellular energy balance are altered by oxidative stress in dysfunctional ECs (Donato et al., 2015). (3) Dietary glycine modulates glutathione biosynthesis, which protects ECs against oxidative stress (Ruiz-Ramirez et al., 2014). (4) Reactive oxygen species (ROS)-scavenging systems such as glutathione peroxidase require reduced glutathione (GSH), which is regenerated from its oxidized form (GSSG) by NADPH-dependent glutathione reductase (Gorrini et al., 2013). Aside from this fragmentary evidence, it remains unknown if and how QECs reprogram their metabolism to adopt a vasculoprotective phenotype.

When QECs become angiogenic, they increase glycolysis to promote migration and proliferation (De Bock et al., 2013). In proliferating ECs (PECs), fatty acid β-oxidation (FAO) is important to sustain the tricarboxylic acid (TCA) cycle in conjunction with an anaplerotic carbon source to support nucleotide synthesis (Schoors et al., 2015), while ECs forming a vascular network in a matrix also upregulate FAO (Patella et al., 2015). In contrast, FOXO1, promoting growth arrest, decreases glycolysis in ECs (Wilhelm et al., 2016). Hence, one might expect that QECs would be hypometabolic, although this remains untested. Here, we characterized how ECs reprogram their metabolism when switching from proliferation to quiescence.

RESULTS

Transcriptomic Signature of Metabolic Genes in Quiescent Endothelial Cells

To induce quiescence of ECs, we used two complementary methods. We cultured human umbilical vein endothelial cells (referred to hereafter as "ECs") until they were contact inhibited (Noseda et al., 2004), or stimulated ECs with Dll4 to activate pro-quiescent Notch signaling (Harrington et al., 2008), yielding similar results. With either approach, fewer ECs proliferated, while more cells resided in the G_0 phase (Figures 1A and S1A) and elevated the expression of downstream Notch-target genes (Figures S1B and S1C), without signs of senescence (Figure S1D). We assessed global metabolic changes induced by quiescence by performing an unbiased transcriptomics analysis in proliferating ECs (PECs) versus quiescent ECs (QECs), focusing on the 1,444 detected metabolic genes. Correlation heatmap analysis and hierarchical clustering revealed that QECs and PECs grouped into distinct metabolic clusters ($p < 0.05$), indicating different metabolic gene signatures (Figure 1B).

QECs Upregulate Fatty Acid Oxidation

Cell quiescence has been associated with cellular hypometabolism (Wilhelm et al., 2016). Surprisingly, therefore, of the ten self-contained gene sets of central carbon metabolism, rotation gene set test (ROAST) analysis revealed that FAO was the only significantly upregulated pathway and had the highest fraction of upregulated genes of all pathways in central metabolism (false discovery rate-adjusted $p = 1.00 \times 10^{-4}$). An opposite effect or trend was observed for glycolysis, serine biosynthesis, TCA cycle, oxidative phosphorylation (OXPHOS), and nucleotide and fatty acid synthesis (Table S1). By heatmap and pathway mapping analysis, QECs upregulated transcripts of various FAO genes (some only modestly), while lowering transcripts of genes involved in glycolysis, TCA cycle, purine/pyrimidine synthesis, and pathways contributing to nucleotide synthesis (non-oxidative pentose phosphate pathway, one-carbon metabolism) (Figures 1C, 1D, and S1E; see Tables S2 and S3 for full name of genes), consistent with their lower proliferation rate and anabolic need (Figure 1A). Since PECs utilize FAO to support nucleotide synthesis (Schoors et al., 2015), we had expected that QECs would have lower, not higher FAO levels, since QECs synthesize fewer nucleotides as they proliferate less. We therefore focused on the surprising finding that FAO gene expression was higher in QECs than in PECs.

Endothelial Cells Increase FAO Flux when Becoming Quiescent

FAO flux increased when ECs became quiescent, up to 3- to 4-fold higher than in PECs (Figures 2A, 2B, and S2A), while glycolytic flux and glucose consumption were reduced (Figures 2A, 2C, 2D, and S2B). Glucose and glutamine oxidation, and fatty acid synthesis were also reduced in QECs (Figures 2E–2G

Figure 1. Metabolic Transcriptomics of QECs versus PECs

(A) Percentage of EdU^{neg} cells (left) and [^{3}H]thymidine incorporation into DNA (proliferation assay; right) in contact-inhibited QECs and PECs (n = 3). DPM, disintegrations per minute. Statistics: mixed models statistics. Data are mean ± SEM; *$p < 0.05$.

(B) Correlation heatmap and hierarchical cluster analysis of transcript levels of 1,444 metabolic genes of central carbon metabolism in QECs versus PECs (n = 4 biological replicates with 3 technical replicates each). Color scale: red, high correlation; blue, low correlation.

(C) Heatmap of transcript levels of FAO, oxPPP, non-oxPPP, and glycolytic genes in contact-inhibited QECs and PECs (n = 4 biological replicates with 3 technical replicates each). Color scale: red, high correlation; blue, low correlation.

(D) Pathway map showing changes in transcript levels of genes in central carbon metabolism in QECs relative to PECs. Color scale: red, upregulated genes by at least 15%; gray: unchanged, change <15%; blue: downregulated by at least 15%. For full gene names, see Tables S2 and S3.

See also Figure S1 and Tables S1, S2, and S3.

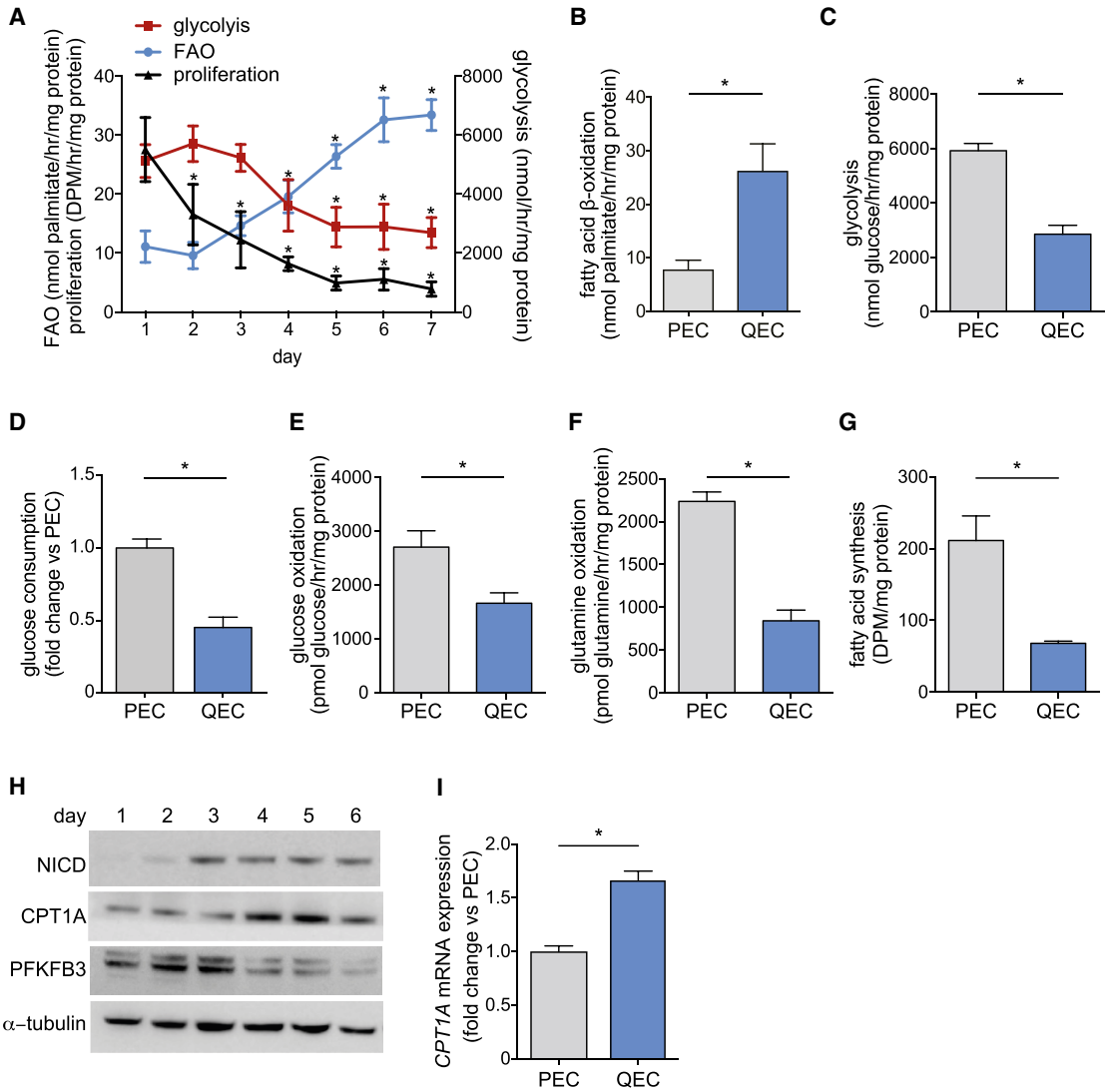

Figure 2. Metabolic Adaptations upon Induction of EC Quiescence

(A) Progressive changes of EC metabolism (glycolysis, red; FAO, blue) and proliferation ([^{3}H]thymidine incorporation, black) during induction of contact-inhibited EC quiescence (n = 4).

(B–F) FAO (B), glycolytic rate (C), glucose consumption (D), glucose oxidation (E), and glutamine oxidation (F) in contact-inhibited QECs versus PECs (n = 3–8).

(G) Fatty acid synthesis measured by [U-^{14}C]acetate incorporation in fatty acids, in QECs versus PECs (n = 4).

(H) Representative immunoblot (n = 5) for NICD, CPT1A, and PFKFB3 during induction of EC quiescence by contact inhibition. α-Tubulin was used as loading control. For densitometric quantifications, see Table S4.

(I) qRT-PCR analysis of *CPT1A* in contact-inhibited QECs relative to PECs (n = 5).

In (A) and (H), proliferating ECs (day 1) are standard proliferating cultures. In (B) to (G) and (I), PECs were obtained by reseeding QECs, which initiates cell proliferation. DPM, disintegrations per minute. Statistics: mixed models statistics (A–C and E–G), two-tailed t test with Welch correction (D and I). Data are mean ± SEM; *p < 0.05 versus day 1 (A) or versus PEC (B–G and I). See also Figures S2 and S3; Tables S4 and S5.

and S2C–S2E). Expression of CPT1A, a rate-controlling enzyme of FAO (Schoors et al., 2015), was increased, while that of PFKFB3, a glycolytic activator (De Bock et al., 2013), declined when ECs became quiescent (Figures 2H, 2I, S2F, and S2G; Table S4). Similar metabolic changes were detected in arterial ECs (Figures S2H and S2I). Use of other models of EC quiescence, based on exposing ECs to physiological shear stress (Lin et al., 2000), confirmed higher CPT1A expression (Figures S2J and S2K).

FAO Is Dispensable for Energy Homeostasis, Biomass Synthesis, and Histone Acetylation in QECs

As cells use FAO for ATP and acetyl-coenzyme A (CoA) production (Ghesquiere et al., 2014; Xiong et al., 2018), redox homeostasis (Harjes et al., 2016), epigenetic regulation (Wong et al., 2017), or DNA synthesis (Schoors et al., 2015), we assessed for which purpose QECs increased FAO, by comparing QECs versus PECs, and by knockdown of CPT1A (CPT1A^{KD}) using two lentiviral vectors, each expressing a different short hairpin

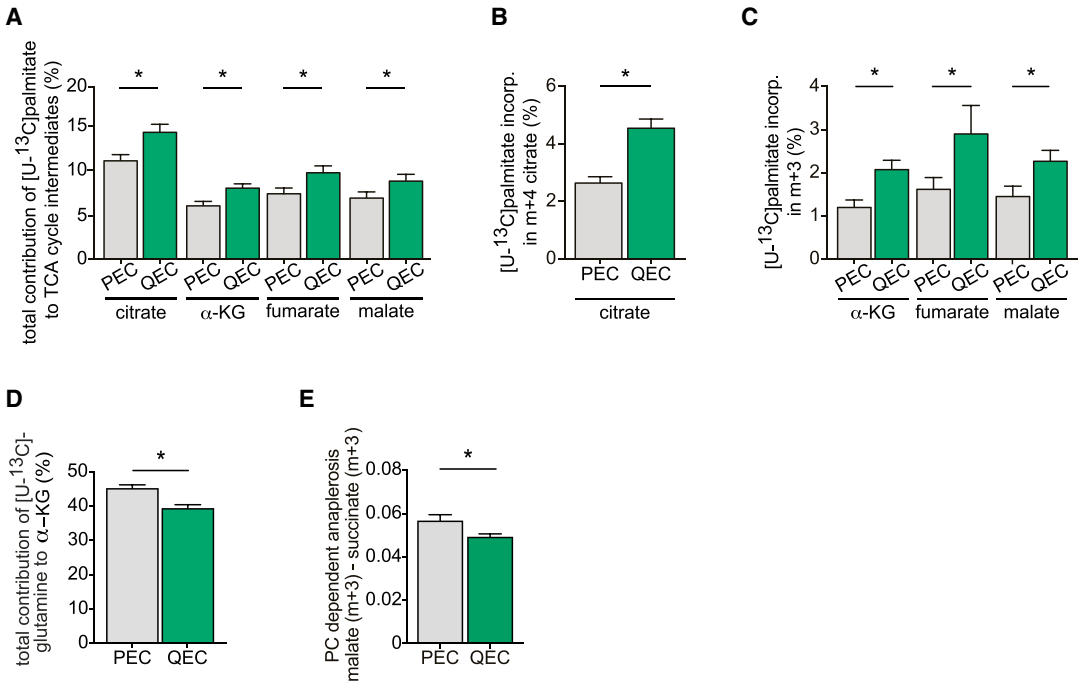

Figure 3. FAO-Derived Carbons Contribute to the TCA Cycle in QECs in Dll4-Induced QECs

(A) Total contribution of [^{13}C]palmitate carbons to the indicated TCA intermediates in QECs versus PECs (n ≥ 4).

(B and C) Analysis of m+4 (B) and m+3 (C) labeled TCA intermediates (from [U-^{13}C]palmitate) in QECs versus PECs (n = 5).

(D) Total contribution of [^{13}C]glutamine carbons to α-KG (n = 3).

(E) Calculation of relative pyruvate carboxylase (PC)-dependent anaplerosis in QECs versus PECs (n ≥ 4). α-KG, α-ketoglutarate.

Statistics: mixed models statistics. Data are mean ± SEM; *p < 0.05.

RNA (Schoors et al., 2015) and reducing CPT1A and FAO levels (Figures S3A–S3C). This combined approach revealed that CPT1A-driven FAO was dispensable for energy homeostasis (Figures S3D–S3I), biomass synthesis (Figures S3J–S3R), and histone acetylation (Figures S3S and S3T; Table S5), and that these processes were not affected by CPT1A^{KD}. We thus explored whether QECs utilized FAO for redox homeostasis.

Increased Contribution of Fatty Acid-Derived Carbons to the TCA Cycle in QECs

To analyze how QECs utilize fatty acids (FAs), we supplemented [U-^{13}C]palmitate and determined ^{13}C-label incorporation into TCA-cycle intermediates, revealing that the total contribution of ^{13}C carbons to TCA-cycle intermediates was higher in QECs than in PECs (Figure 3A). Mass distribution analysis revealed an increase in m+4 citrate and m+3 α-ketoglutarate (αKG), fumarate, and malate in QECs, suggesting that FA-derived carbons sustained an oxidative TCA cycle in QECs (Figures 3B, 3C, and S3U). However, even though QECs used FA-derived carbons to sustain the TCA-cycle flux to a larger extent than PECs, anaplerotic replenishment of the TCA cycle by glutamine and glucose was reduced in QECs, consistent with their lower anabolism (Figures 3D and 3E).

QECs Increase FAO for NADPH Regeneration

In cancer cells, FAO regulates redox homeostasis by generating acetyl-CoA to sustain the TCA cycle (Rohrig and Schulze, 2016; Smolkova and Jezek, 2012). Indeed, the TCA-cycle metabolites (iso)citrate and malate serve as substrates for reactions mediated by isocitrate dehydrogenase (IDH) and malic enzyme (ME) to regenerate NADPH from NADP$^+$ (Rohrig and Schulze, 2016; Smolkova and Jezek, 2012). Transcript levels of mitochondrial IDH2 and ME3 were higher in QECs (Figures 4A and 4B), and partial knockdown of IDH2 and ME3 increased the NADP$^+$/NADPH ratio in QECs (Figures S4A and S4B; more complete knockdown was toxic). NADPH levels were higher in QECs (Figure 4C), while CPT1A^{KD} lowered the elevated NADPH levels in QECs to levels observed in PECs, and increased the NADP$^+$/NADPH ratio (Figures 4C and S4C). CPT1A^{KD} did not affect NADPH regeneration in PECs (Figure 4C), consistent with findings that PECs do not use FAO for redox homeostasis (Schoors et al., 2015). QECs expressed higher transcript levels of genes involved in NAD(P) production, including nicotinamide N-methyltransferase (NNMT), nicotinate phosphoribosyltransferase (NAPRT), NAD synthetase 1 (NADSYN1), and nicotinamide riboside kinase 1 (NMRK1) (Figure 4D). Thus, the elevated NADPH levels in QECs result from a combined effect on increased NADP$^+$ synthesis and on regeneration of NADPH from NADP$^+$ by the increased use of FA-derived carbons to sustain the TCA cycle.

QECs Have Reduced Oxidative Stress

Since NADPH is used by glutathione reductase to convert oxidized glutathione (GSSG) to its reduced form (GSH), a key cellular anti-oxidant, we measured GSSG, GSH, and ROS levels

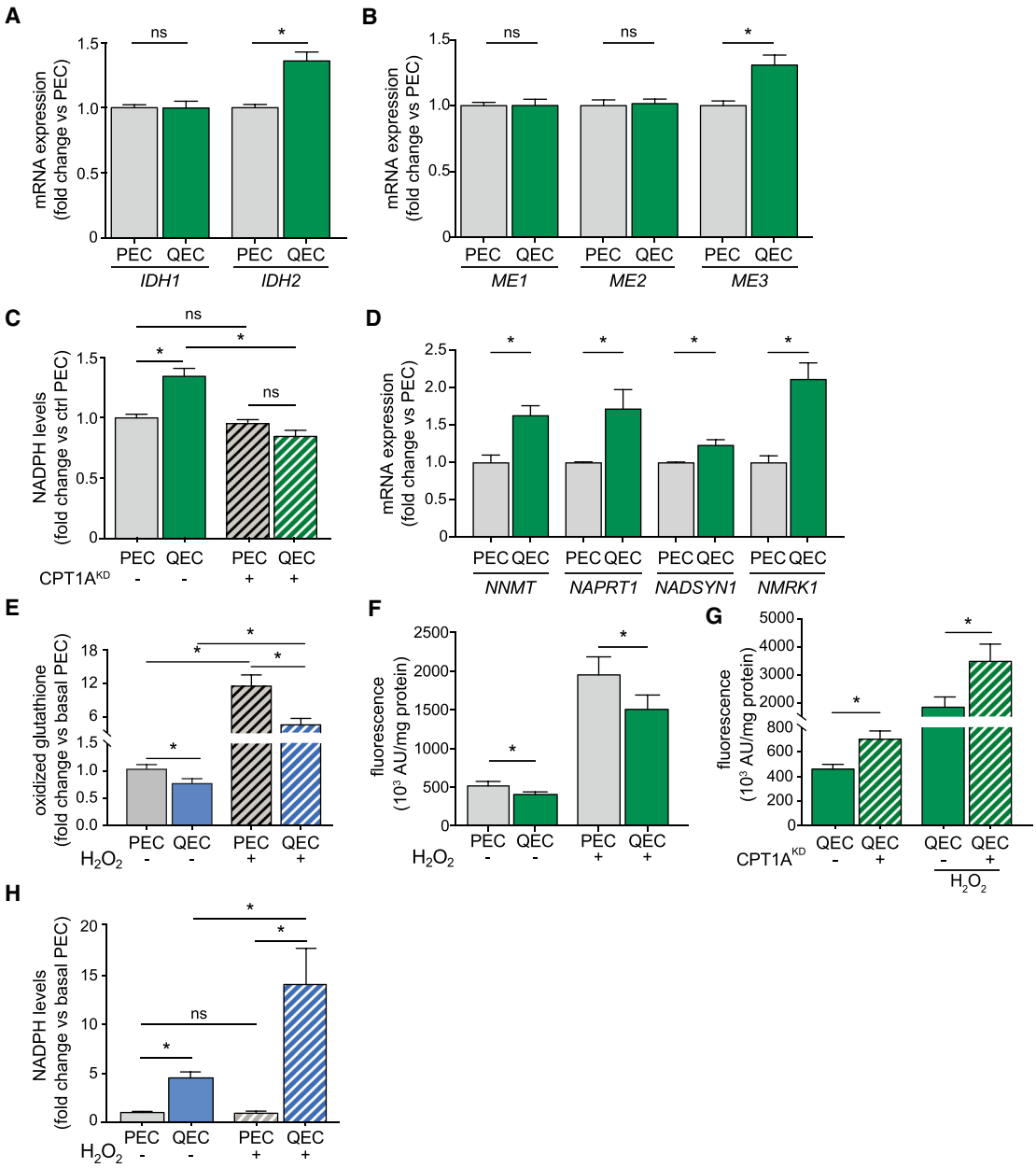

Figure 4. Role of FAO in Redox Homeostasis

(A and B) qRT-PCR analysis of *IDH1*, *IDH2* (A), and *ME1*, *ME2*, *ME3* (B) in QECs relative to PECs ($n \geq 3$).

(C) Total intracellular NADPH levels in ctrl and CPT1A^{KD} QECs or PECs ($n = 3$).

(D) qRT-PCR analysis of *NNMT*, *NAPRT1*, *NADSYN1*, and *NMRK1* in QECs relative to PECs ($n \geq 3$).

(E–H) Oxidized glutathione levels (percent of total GSSG + GSH, expressed relative to PECs) in PECs and contact inhibition-induced QECs (E, $n = 3$), intracellular ROS levels (CM-H_2DCFDA fluorescence) in PECs and QECs (F, $n = 8$), intracellular ROS levels (CM-H_2DCFDA fluorescence) of ctrl or CPT1A^{KD} QECs (G, $n = 5$), and total intracellular NADPH levels (H, $n = 3$) in PECs and contact inhibition-induced QECs, in baseline and upon supplementation with H_2O_2 (50 μM, 2 hr). Unless otherwise indicated, all experiments were performed using the Dll4-induced quiescence model. AU, arbitrary units.

Statistics: two-tailed t test with Welch correction (A, B, and D), ANOVA and Bonferroni post hoc test (C, E, and H), mixed models statistics (F and G). Data are mean ± SEM; ns, not significant; *$p < 0.05$. See also Figure S4.

in baseline conditions and upon exposure to exogenous H_2O_2 (a measure of the cell's capacity to cope with elevated oxidative stress) (referred to as "stress conditions"). Levels of GSSG (percent of total GSSG + GSH) and cellular ROS were lower in QECs in baseline and stress conditions (Figures 4E and 4F). In line with this, CPT1A^{KD} in QECs increased ROS and GSSG levels, supporting a role of FAO in counteracting oxidative stress (Figures 4G and S4D). Unlike PECs, QECs increased NADPH regeneration while maintaining a lower NADP$^+$/NADPH ratio in baseline and stress conditions (Figures 4H and S4E). Silencing

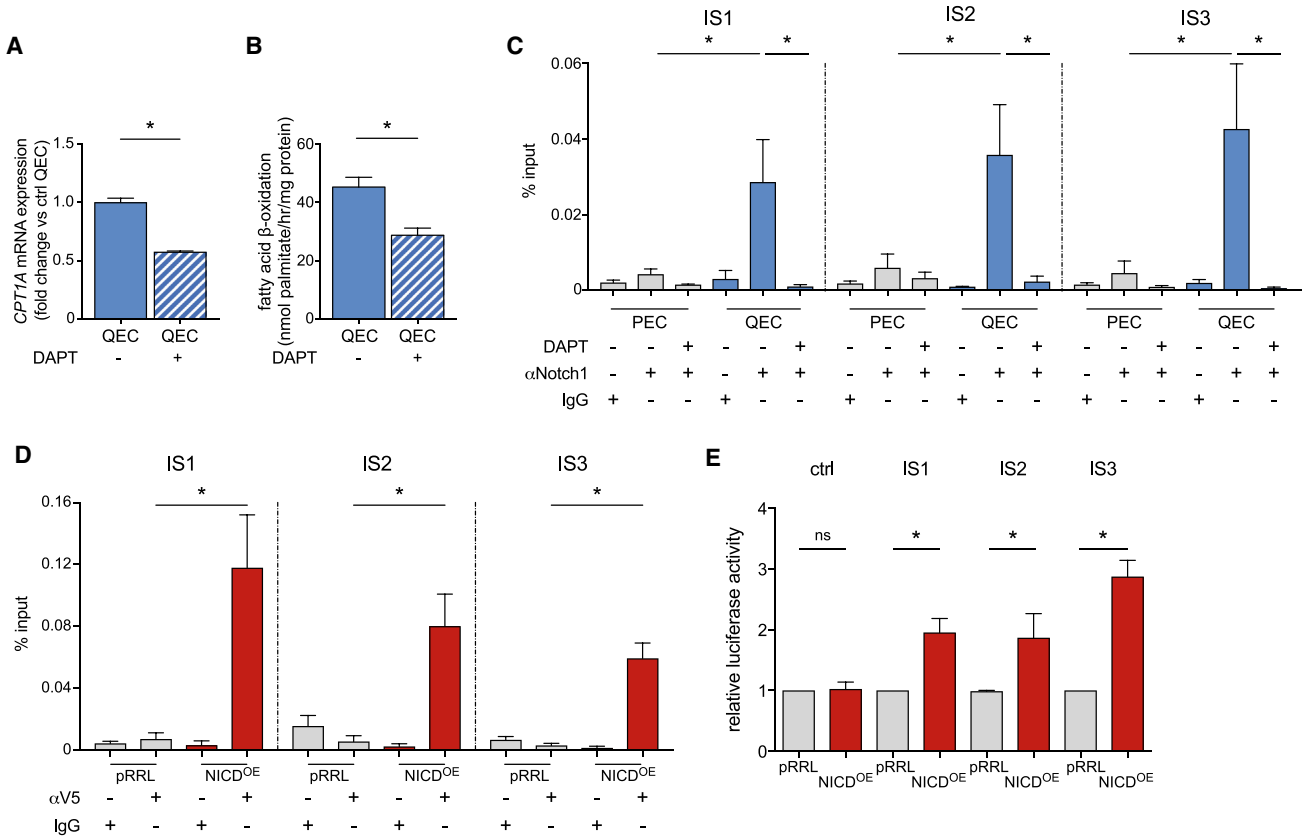

Figure 5. Effect of Notch Signaling on CPT1A Expression

(A) qRT-PCR analysis of *CPT1A* in QECs without or with treatment with DAPT (n = 3).

(B) FAO in QECs without or with treatment with DAPT (n = 8).

(C) ChIP-qPCR analysis of NICD binding to the *CPT1A* promoter at the NICD-RBPjκ consensus interaction site (IS) 1, 2, or 3, in PECs or QECs, treated or not with DAPT and pulled down with anti-Notch1 (αNotch1) or immunoglobulin G (IgG) antibody. Data are presented as percentage of input (n = 4).

(D) ChIP-qPCR analysis of NICD binding to the *CPT1A* promoter at the binding site (IS) 1, 2, or 3 in control ECs (pRRL) and in ECs overexpressing V5-tagged NICD ($NICD^{OE}$). Samples were pulled down with anti-V5 (αV5) or IgG antibody and the data are presented as percentage of input (n = 4).

(E) Relative luciferase activity of reporter constructs driven by a minimal promoter alone (ctrl) or together with NICD-RBPjκ interaction site 1, 2, or 3 of the *CPT1A* promoter, in control or $NICD^{OE}$ ECs (n = 3).

Unless otherwise indicated, all experiments were performed using the contact inhibition-induced quiescence model. Statistics: two-tailed t test with Welch correction (A), mixed models statistics (B), ANOVA and Bonferroni post hoc test (C and D), two-tailed t test with Welch correction and one sample t test (E). Data are mean ± SEM; *p < 0.05; ns, not significant. See also Figure S5.

of *ACADvl* and *HADHB* ($ACADvl^{KD}$/$HADHB^{KD}$) (catalyzing critical steps of FAO) similarly increased ROS levels (Figures S4F–S4H), indicating that FAO, and not only CPT1A-mediated fatty acid import in mitochondria, controls redox homeostasis in QECs.

As different species of ROS such as superoxide ($O_2^{\cdot-}$), hydrogen peroxide (H_2O_2), or hydroxyl radical (OH°) may have different biological functions (Birben et al., 2012; Schieber and Chandel, 2014), yet excess of each of them can trigger EC dysfunction (Incalza et al., 2018), we characterized the ROS species. Use of complementary assays revealed that mitochondrial/cellular levels of $O_2^{\cdot-}$, H_2O_2, and OH° were all reduced in QECs (Figures S4I–S4O). Overall, QECs are better equipped to scavenge ROS and to cope with oxidative stress.

Molecular Mechanism of Upregulation of FAO in QECs

As QECs upregulated Notch signaling and Notch activation promoted EC quiescence (see above), we focused on Notch as a possible transcriptional activator of CPT1A gene expression in QECs. Blocking Notch signaling with DAPT (N-[N-(3,5-difluorophenacetyl)-L-alanyl]-S-phenylglycine t-butyl ester) in QECs decreased CPT1A expression and FAO flux (Figures 5A and 5B). We then investigated whether Notch signaling increased CPT1A transcription. The transcriptionally active Notch intracellular domain (NICD) does not bind to DNA directly, but only via interaction with RBPJκ, a DNA-binding protein (Castel et al., 2013). Notably, we identified four putative RBPJκ-binding motifs (Castel et al., 2013) in close proximity to the start codon of the CPT1A gene (referred to as interaction site 1 [IS1], IS2, IS3, and IS4) (Figure S5A).

Chromatin immunoprecipitation (ChIP)-qPCR analysis, using an anti-Notch1 (αNotch1) antibody that captures NICD, revealed an interaction of NICD with three of the four identified sites (IS1, IS2, and IS3) in QECs, which was reduced upon treatment with DAPT (Figures 5C, S5B, and S5C). We also

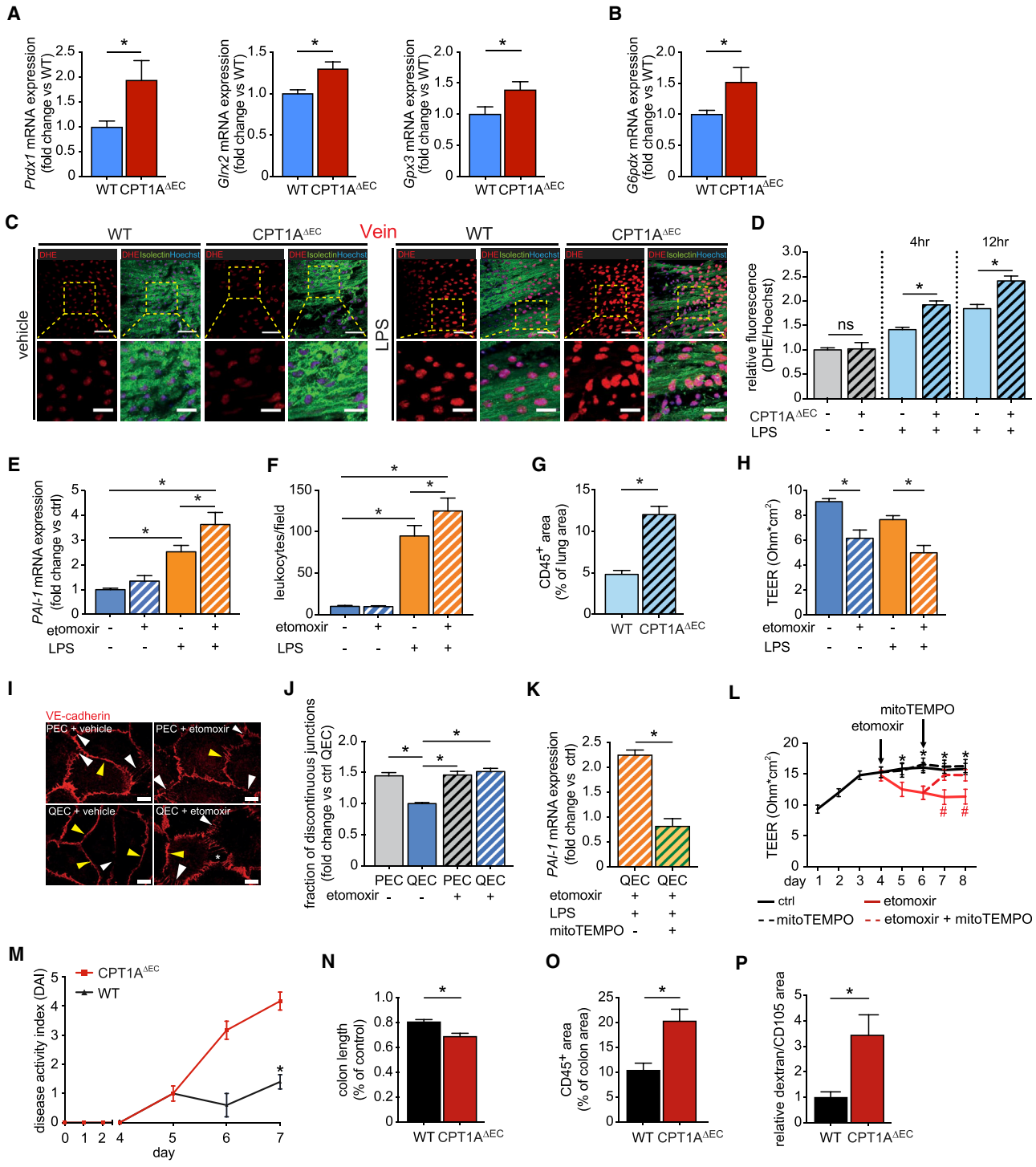

Figure 6. Role of FAO in EC Barrier Function and Vasculoprotection *In Vivo* and *In Vitro*

(A and B) qRT-PCR analysis of enzymes involved in glutathione metabolism (*Prdx1*, *Glrx2*, and *Gpx3*) (A) and enzymes of the pentose phosphate pathway (PPP) (*G6pdx*) (B) in ECs freshly isolated from wild-type (WT) and EC-specific CPT1A knockout (CPT1A$^{\Delta EC}$) mice (n $\geq$ 3).

(C and D) $O_2^{\cdot -}$ formation in the portal vein in WT and CPT1A$^{\Delta EC}$ mice at 4 and 12 hr after injection of vehicle (PBS) or LPS, evaluated by staining for the oxidative fluorescent dye dihydroethidium (DHE). (C) Representative photomicrographs of portal vein open book preparations from the 12-hr treated mice, stained for DHE (red), the EC marker isolectin B4A (green), and nuclei (Hoechst; blue). Lower panels show larger magnifications of the boxed areas in the upper panels. (D) Quantification of DHE fluorescence signal normalized for Hoechst fluorescence, and expressed relative to control (n = 3 independent experiments, each comprising n > 4 mice per group).

(E) qRT-PCR analysis of *PAI-1* in QECs upon single or combined treatment with etomoxir and LPS (to induce oxidative stress) (n = 4).

(legend continued on next page)

tested ECs overexpressing V5-tagged NICD ($NICD^{OE}$), which, as expected (given that Notch is a pro-quiescent signal), were more quiescent, and had increased levels of FAO and CPT1A transcripts (Figures S5D–S5G). Use of an anti-V5 tag antibody (αV5) showed that NICD interacted with IS1, IS2, and IS3 in $NICD^{OE}$ but not control ECs (Figures 5D, S5H, and S5I). Cloning of the CPT1A fragments, containing the IS1, IS2, and IS3 sequences, in luciferase reporter constructs with a minimal promoter confirmed that $NICD^{OE}$ enhanced the luciferase activity, as a parameter of increased CPT1A gene transcription (Figure 5E). Thus, Notch signaling upregulates FAO flux, at least in part via induction of CPT1A gene expression. Similar analyses showed that Notch regulated the expression of IDH2 and ME3, involved in NADPH regeneration and redox homeostasis in QECs (Figures S5J and S5K).

FAO Inhibition due to Loss of CPT1A in QECs Causes Oxidative Stress *In Vivo*

To translate our *in vitro* findings, we used two *in vivo* approaches: (1) adult 8-week-old mice (containing only/primarily QECs) with a conditional inactivation of CPT1A in ECs (Cdh5(PAC)-Cre^{ERT2}-$CPT1A^{lox/lox}$ mice) upon tamoxifen treatment (referred to as "$CPT1A^{\Delta EC}$ mice") (Schoors et al., 2015) (Figures S6A and S6B); and (2) young P8 mice (in which growing blood vessels contain both PECs and QECs) treated with etomoxir, an irreversible pharmacological blocker of CPT1 that lowers FAO levels in ECs (Schoors et al., 2015).

RNA sequencing or RT-PCR analysis showed that freshly isolated $CPT1A^{\Delta EC}$ QECs upregulated the expression of genes involved in redox homeostasis, presumably to restore redox homeostasis. Gene set enrichment analysis and pathway mapping revealed that glutathione metabolism, a key pathway in redox homeostasis, ranked among the top three most upregulated pathways in QECs of $CPT1A^{\Delta EC}$ mice ($p = 0.0017$; $p_{adjusted} = 0.03$) (Figure S6C and Table S6). RT-PCR confirmed the upregulation of enzymes involved in ROS scavenging (e.g., peroxiredoxin-1 [*Prdx1*], mitochondrial glutaredoxin-2 [*Glrx2*], glutathione peroxidase 3 [*Gpx3*]) (Figure 6A). Also, the rate-controlling enzyme of the oxidative PPP (pentose phosphate pathway; glucose-6-phosphate dehydrogenase [G6pdx]), generating NADPH in the cytosol, was upregulated in $CPT1A^{\Delta EC}$ QECs (Figure 6B), in line with an increased oxPPP flux in QECs upon $CPT1A^{KD}$ (Figure S6D). Thus, $CPT1A^{\Delta EC}$ QECs upregulate metabolic pathways producing NADPH, presumably to restore redox homeostasis.

We then assessed whether $CPT1A^{\Delta EC}$ QECs elevated ROS levels in intact vessels by staining for the ROS marker dihydroethidium (DHE) and the EC marker isolectin using the aorta and portal vein open book preparation (Sumiyoshi et al., 2008). DHE levels were comparable in ECs in wild-type (WT) and $CPT1A^{\Delta EC}$ mice in baseline conditions (Figures 6C, 6D, S6E, and S6F). However, upon administration of lipopolysaccharide (LPS), which induces EC dysfunction, vascular damage, and leakage because of ROS production (Kratzer et al., 2012), intracellular ROS levels in QECs were higher in $CPT1A^{\Delta EC}$ mice (Figures 6C, 6D, S6E, and S6F). Thus, CPT1A gene loss in QECs elevated ROS levels *in vivo* and rendered them more prone to oxidative stress upon an inflammatory insult, known to cause EC dysfunction.

To provide evidence for the dual role of FAO in PECs (proliferation) versus QECs (redox homeostasis) simultaneously occurring in a single tissue ("mixed model"), we analyzed freshly isolated ECs from growing vessels of different organs (heart, lung, and liver) in control or etomoxir-treated P8 mice upon 5-ethynyl-2′-deoxyuridine (EdU) injection to identify EdU^{pos} PECs and EdU^{neg} QECs by flow cytometry; we measured cellular ROS levels by flow cytometry upon DHE staining. This analysis showed that, consistent with our previous findings (Schoors et al., 2015), etomoxir reduced the fraction of PECs, thus rendering the endothelium more quiescent (Figure S6G). Coincidentally, ROS levels in isolated ECs were increased upon etomoxir treatment (Figure S6H). Given that the large majority of ECs were EdU^{neg} QECs and etomoxir further expanded this population, FAO inhibition elevated oxidative stress in QECs also in this mixed model containing both PECs and QECs.

FAO Inhibition Causes EC Dysfunction due to Oxidative Stress

EC dysfunction due to oxidative stress is characterized by a higher pro-thrombotic state, increased adhesiveness of inflammatory leukocytes, and enhanced leakiness (Incalza et al., 2018; Kevil et al., 2000). We assessed *in vitro* if FAO inhibition

(F) Leukocyte adhesion to a QEC monolayer upon single or combined treatment with etomoxir and LPS (n = 3).
(G) Quantification of $CD45^+$ cells in the lungs of WT and $CPT1A^{\Delta EC}$ mice, 4 hr after injection of LPS (n = 6).
(H) TEER analysis of QEC monolayers upon single or combined treatment with etomoxir and LPS (n = 3).
(I) Representative images of QECs and PECs, stained for VE-cadherin (red), without (vehicle) or with etomoxir treatment. White arrowheads denote discontinuous junctions; yellow arrowheads denote continuous junctions; asterisk denotes a gap between ECs resulting from discontinuous junctions.
(J) Quantification of discontinuous junctions in quiescent QECs versus PECs without (vehicle) or with etomoxir treatment (n = 3).
(K) qRT-PCR analysis of *PAI-1* in QECs upon treatment with etomoxir and LPS (to induce oxidative stress) and with or without the ROS scavenger mitoTEMPO (n = 3).
(L) TEER measurements over 8 consecutive days, without (black lines) or with etomoxir treatment (red lines) and without (solid lines) or with subsequent mitoTEMPO treatment (dashed lines) (n = 5). Arrows indicate initiation of treatments.
(M) Disease activity index (DAI) of colitis in WT and $CPT1A^{\Delta EC}$ mice during treatment with 2.5% DSS in their drinking water for 7 consecutive days (n = 7).
(N) Colon length of WT and $CPT1A^{\Delta EC}$ mice after DSS treatment. The values are expressed relative to vehicle-treated control group (n = 7).
(O) $CD45^+$ cell infiltration in the colon wall in WT and $CPT1A^{\Delta EC}$ mice after DSS treatment (n = 7).
(P) Quantification of vascular leakiness (histological analysis of extravascular dextran) in WT and $CPT1A^{\Delta EC}$ mice after DSS treatment (n = 7).
All *in vitro* experiments were performed using the contact inhibition-induced quiescence model. Since $CPT1A^{KD}$ reduces EC proliferation, precluding these cells to form a monolayer of contact-inhibited QECs, we treated contact-inhibited QEC with etomoxir in order to inhibit FAO in (E), (F), and (H) to (L). Statistics: two-tailed t test with Welch correction (A, B, D, G, K, and M–P), ANOVA and Bonferroni post hoc test (E, F, and J), mixed models statistics (H and L). Data are mean ± SEM; ns, not significant, *$p < 0.05$ and #$p < 0.05$. In (L) asterisks (*) denote statistical differences between control and etomoxir, hashtags (#) between etomoxir and etomoxir plus mitoTEMPO. Scale bars, 50 μm (C, upper panels), 20 μm (C, lower panels), and 100 μm (I). See also Figure S6 and Table S6.

by etomoxir promoted QEC activation/dysfunction, in baseline conditions and upon treatment with LPS. First, compared with control, QECs treated with etomoxir tended to have increased mRNA levels of the anti-fibrinolytic enzyme plasminogen activator inhibitor 1 (*PAI-1*) at baseline, a difference that became significant upon exposure to LPS (Figure 6E). Second, etomoxir increased leukocyte adhesion upon activation of QECs with LPS (Figure 6F). In agreement, infiltration of $CD45^+$ leukocytes into the lungs of $CPT1A^{\Delta EC}$ mice was increased upon LPS administration (Figure 6G). $CPT1A^{\Delta EC}$ mice were more sensitive to LPS, as they died earlier than WT mice, indicating that reduced FAO in QECs aggravates the response to LPS (Figure S6I). In line with this, at 24 hr after LPS injection the serum levels of pro-inflammatory cytokines (interferon-γ [INFγ], tumor necrosis factor α [TNFα], interleukin-5 [IL-5], IL-17, IL-23) were higher in $CPT1A^{\Delta EC}$ mice (Figure S6J), likely contributing to the shorter survival. Third, trans-endothelial electrical resistance (TEER) was lower (reflecting decreased barrier function) in etomoxir-treated QECs, in both baseline and LPS conditions (Figure 6H). In agreement, etomoxir-treated QECs contained fewer VE-cadherin$^+$ continuous stable adherens junctions, in which VE-cadherin is localized linearly along cell-cell borders (Figures 6I and 6J). Accordingly, treatment of QECs with trimetazidine (TMZ), inhibiting long-chain 3-ketoacyl-CoA thiolase (encoded by *HADHB*), increased oxidative stress and endothelial permeability, as demonstrated by reduced TEER levels (Figure S6K), and increased discontinuous VE-cadherin$^+$ junctions (Figure S6L).

To assess the role of ROS, we supplemented QECs with mitoTEMPO, a scavenger of mitochondrial ROS. The induction of *PAI-1* expression in etomoxir and LPS pre-treated QECs was reduced to control levels after exposure to mitoTEMPO (Figure 6K). Also, mitoTEMPO treatment of etomoxir-treated QECs rescued the increased leakiness induced by blocking CPT1A in QECs (Figure 6L). Together, FAO is a safeguard for QECs to maintain redox homeostasis, and inhibition of FAO predisposes QECs to activation and dysfunction when exposed to oxidative stress.

FAO Inhibition Accelerates DSS-Induced Colitis

To provide additional evidence for a role of FAO in QEC homeostasis, we used a model of inflammatory bowel disease (IBD). The gut-vascular barrier (GVB) is normally impermeable but becomes leaky in IBD, thus promoting leukocyte infiltration and aggravating disease progression (Cibor et al., 2016). Oxidative stress plays a key role in IBD by increasing GVB permeability (Tian et al., 2017). In addition to leukocytes (the major source of ROS), ECs also produce ROS in IBD (Oshitani et al., 1993). We thus hypothesized that the decreased capacity of $CPT1A^{\Delta EC}$ QECs to scavenge ROS (produced by QECs or other sources) might aggravate permeability, infiltration of leukocytes, and overall susceptibility to dextran sodium sulfate (DSS)-induced colitis.

The disease activity index (DAI) (scoring body weight loss, stool consistency, and blood in the stool and anal region) was more severe in $CPT1A^{\Delta EC}$ mice (Figure 6M). Also, in $CPT1A^{\Delta EC}$ mice, colons shrunk more (Figures 6N and S6M) and displayed more severe histological signs of colitis, including loss of crypts, separation of the crypt base from the muscularis mucosa and colonic wall thickening (Figure S6N), more pronounced infiltration of $CD45^+$ leukocytes in colons (Figure 6O), and increased vascular leakiness resulting from a breached QEC barrier (Figure 6P). At the same time, neovessels formed in the inflamed colonic mucosa, thus representing a "mixed model." In line with previous findings (Schoors et al., 2015), the vessel area and fraction of proliferating $PCNA^+$ PECs were reduced in $CPT1A^{\Delta EC}$ mice (Figures S6O and S6P), confirming that FAO has different biological roles in PECs versus QECs in a single tissue.

Acetate Supplementation Lowers Oxidative Stress in QECs of $CPT1A^{\Delta EC}$ Mice

Finally, we explored a possible translational therapeutic potential. We hypothesized that supplementation of acetate (metabolized to acetyl-CoA, a downstream product of FAO) might lower ROS levels in QECs, a finding of therapeutic relevance to counter EC dysfunction. Acetate supplementation of QECs (exposed to H_2O_2) prevented the increase in ROS levels upon CPT1A silencing (Figure 7A). Also, treating $CPT1A^{\Delta EC}$ mice with sodium acetate prevented the increase in DHE^+ ROS levels in QECs upon LPS treatment (Figures 7B and 7C) and reduced infiltration of $CD45^+$ leukocytes into the lungs (Figure 7D). Control experiments showed that mitochondrial conversion of acetate to acetyl-CoA is essential for the rescue by acetate (Figures S7A–S7G and Table S7).

DISCUSSION

Quiescent ECs Use FAO for Redox Homeostasis

QECs are not hypometabolic, but increase FAO, up to 3- to 4-fold, the largest change of any metabolic pathway flux we observed in healthy ECs to date (De Bock et al., 2013; Huang et al., 2017; Schoors et al., 2015; Wong et al., 2017). QECs did not rely on FAO for ATP production, nucleotide synthesis, or histone acetylation, unlike PECs that utilize FAO to sustain DNA synthesis (Schoors et al., 2015), or lymphatic ECs that use FAO for epigenetic regulation of lymphatic gene expression (Wong et al., 2017).

Instead, QECs utilize FAO for redox homeostasis, partly by regenerating $NADP^+$ to NADPH likely at the IDH2 and ME3 reaction steps. However, QECs also upregulate the expression of genes involved in $NADP^+$ production, contributing to improved redox homeostasis. The importance of CPT1A-driven FAO for redox homeostasis of QECs *in vivo* was supported by evidence that ROS levels were elevated after LPS challenge in QECs of $CPT1A^{\Delta EC}$ mice. As a consequence of the ROS-mediated induction of EC barrier dysfunction, leukocyte infiltration into the lung was increased and survival of $CPT1A^{\Delta EC}$ mice was compromised. A similar outcome was observed when $CPT1A^{\Delta EC}$ mice were challenged with DSS-induced colitis.

By using FAO for redox homeostasis, QECs differ from other non-transformed cell types. Indeed, certain immune, glial, and neural stem cells rely on FAO for energy production (Ghesquiere et al., 2014; Stoll et al., 2015), but not for redox balance. Opposite to the anti-oxidant role of FAO in QECs, M1-like macrophages even use FAO for the production of bactericidal mitochondrial ROS (Ghesquiere et al., 2014). Only some cancer cells utilize FAO for redox control (Harjes et al., 2016), although

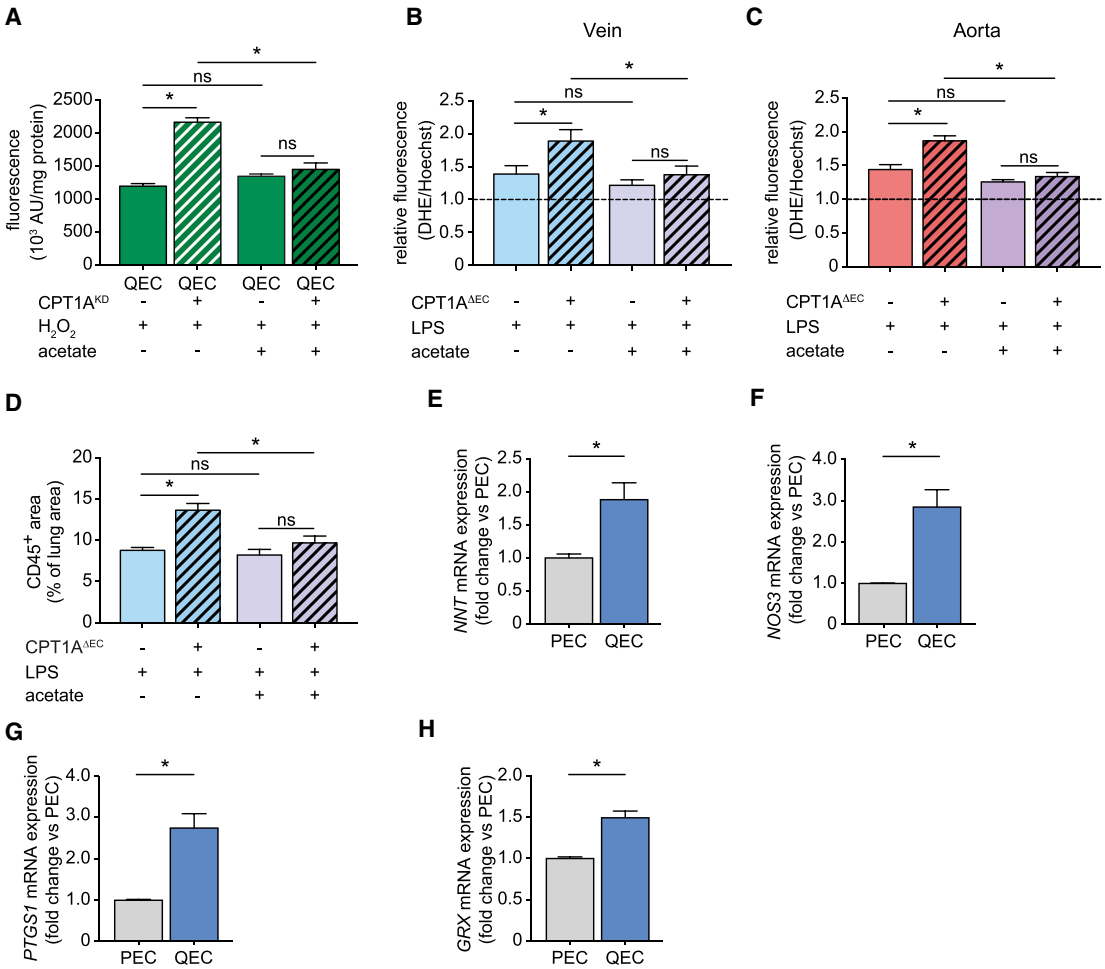

Figure 7. Effect of Acetate Supplementation on Oxidative Stress in Quiescent ECs *In Vivo* and *In Vitro*, and Vasculoprotective Gene Expression in PECs versus QECs

(A) Intracellular ROS levels (CM-H_2DCFDA fluorescence) of ctrl and CPT1A^{KD} QECs, with or without acetate supplementation, upon exposure to H_2O_2 (50 μM, 2 hr) (n = 5; Dll4 induced quiescence model). AU, arbitrary units.

(B and C) Quantification of $O_2^{\cdot-}$ formation (DHE fluorescence normalized for Hoechst fluorescence) of portal vein (B) and aorta (C) open book preparations in WT or CPT1A$^{\Delta EC}$ mice, at 12 hr after injection with vehicle (PBS) or LPS, with or without acetate treatment (n > 10). Dashed horizontal line, value for untreated WT control.

(D) Quantification of CD45$^+$ cells in the lungs of WT and CPT1A$^{\Delta EC}$ mice with or without acetate treatment, 12 hr after injection of LPS (n > 10).

(E–H) qRT-PCR analysis of *NNT* (E) (n = 5), *NOS3* (F), *PTGS1* (G), and *GRX* (H) in PECs and contact-inhibited QECs (n = 4).

Statistics: mixed models statistics (A), ANOVA and Bonferroni post hoc test (B–D), two-tailed t test with Welch correction (E–H). Data are mean ± SEM; ns, not significant, *p < 0.05. See also Figure S7 and Table S7.

they mostly use FAO for energy production (Qu et al., 2016), epithelial-to-mesenchymal transition (Nath and Chan, 2016), or metastasis (Pascual et al., 2017).

Control of Redox Homeostasis by FAO Counteracts QEC Dysfunction

Oxidative stress promotes EC activation/dysfunction, leading to increased vascular thrombogenicity, leakiness, and inflammation (Incalza et al., 2018; Kevil et al., 2000). Consistent with a role of FAO in EC redox homeostasis, CPT1A inhibition elevated ROS levels, leading to decreased anti-fibrinolytic gene expression, vascular wall leakage *in vitro* and *in vivo*, and increased leukocyte adhesion *in vitro* and infiltration *in vivo*. Notably, treatment of QECs with a mitochondrial anti-oxidant rescued vascular leakage, a key feature of EC dysfunction. Blood vessel-lining QECs are exposed to high levels of oxygen in the blood and thus to an oxidative stress-prone environment, while blood vessel-forming PECs invade avascular, hypoxic areas. We speculate that QECs require a higher level of redox buffering capacity than PECs.

Molecular Mechanism: Notch at a Crossroad

We show that Notch upregulates CPT1A, IDH2, and ME3 expression by interacting with the DNA-binding protein RBPJκ. As such, Notch signaling constitutes a molecular switch (rheostat) that elevates FAO to produce more NADPH in QECs,

although other molecular regulators may also contribute. Notch is known to inhibit DNA synthesis in ECs through induction of the cell-cycle inhibitor $p27^{KIP1}$ and suppression of nuclear translocation of the cell-cycle drivers cyclinD1-cdk4 (Noseda et al., 2004; Rostama et al., 2015). In agreement, we detected lower expression of nucleotide synthesis genes in QECs than PECs. This may explain how Notch signaling redirects the use of FAO from nucleotide synthesis in PECs to NADPH regeneration in QECs. Indeed, by transcriptionally lowering genes involved in nucleotide synthesis, QECs are programmed to no longer use (or use less) TCA-cycle metabolites for nucleotide synthesis. Thus, even though FAO sustains the TCA cycle more in QECs than PECs, QECs are prevented from anabolic synthesis of nucleotides by the cell-cycle inhibitory signaling activity of Notch. Hence, as a metabolic adaptation accompanying the cellular shift to quiescence by Notch, QECs no longer/less use FAO for nucleotide synthesis, even though FAO levels are increased, but rather to sustain the TCA cycle for NADPH regeneration. Our findings highlight the plasticity of how a single cell type (EC) can reprogram the use of the same metabolic pathway (FAO) for either nucleotide synthesis or redox homeostasis, depending on the cellular status (proliferation versus quiescence). Our data are not in conflict with a report that Notch signaling in ECs induces the expression of fatty acid transporters, including FABP4 (Harjes et al., 2014), and that silencing of FABP4 in PECs induces oxidative stress and inhibits tumor angiogenesis (Harjes et al., 2017), since it remains unclear whether FABP4 fuels FAs to FAO and FABP4 has various FAO-independent activities (Furuhashi et al., 2014).

QECs Switch on Additional NADPH-Producing Vasculoprotective Pathways

Interestingly, QECs also upregulated the expression of other NADPH-regenerating pathways, such as the oxidative PPP and nicotine nucleotide transhydrogenase (NNT; converting NADH [produced by FAO] into NADPH) (Figure 7E), as well as $NADP^+$-producing pathways. Notably, QECs also upregulated the expression of enzymes such as eNOS (NOS3), prostaglandin G/H synthase 1 (PTGS1), and glutaredoxin (GRX) (Figures 7F–7H), involved in vasculoprotection against EC dysfunction induced by oxidative stress (Egan and FitzGerald, 2006; Heiss et al., 2015). Remarkably, these vasculoprotective enzymes use NADPH as cofactor (Davidge, 2001; Ulrich et al., 2013). Hence, these findings suggest an appealing model whereby QECs mount a broad vasculoprotective program, relying on enzymes, several of which require/consume NADPH. To meet these increased needs of NADPH, QECs reprogram their metabolism to upregulate NADPH regeneration via several complementary mechanisms, of which FAO is a major contributor.

Possible Translational Implications

Consistent with our findings that QECs, exposed to high oxygen levels and thus prone to oxidative stress, require FAO to secure redox homeostasis, human QECs expressed higher CPT1A levels in the highly oxygenated than in the poorly oxygenated tissues tested (Figures S7H and S7I). Moreover, our findings that acetate supplementation restored the ROS-scavenging potential of CPT1A-silenced ECs in the LPS model and normalized the elevated endothelial ROS levels and leukocyte infiltration in mice lacking endothelial CPT1A suggest that promoting FAO or stimulating the use of acetate-derived carbons might be beneficial to counteract EC dysfunction in disease. Given that EC dysfunction has been postulated to contribute to multiple diseases, in fact more than the dysfunction of other cell types (Dahlman et al., 2014), identifying such metabolite-based strategies to counteract/prevent EC dysfunction through improved anti-oxidant control, might possibly offer therapeutic opportunities.

Limitations of the Study

Our data highlight that FAO is indispensable for maintaining redox homeostasis in ECs. Using two different disease models, we document that loss of CPT1A in ECs induces EC dysfunction resulting from elevated oxidative stress. Our data also indicate that acetate treatment is capable of counteracting redox imbalance in conditions of CPT1A suppression. It will be interesting to explore further whether inadequate FAO levels contribute to diseases characterized by EC dysfunction due to oxidative stress, and whether acetate supplementation might have therapeutic potential in counteracting imbalanced oxidative stress, EC dysfunction, and progression of these diseases.

STAR★METHODS

Detailed methods are provided in the online version of this paper and include the following:

- KEY RESOURCES TABLE
- CONTACT FOR REAGENT AND RESOURCE SHARING
- EXPERIMENTAL MODEL AND SUBJECT DETAILS
  - Mice
  - Cell Isolation and Culture
- METHOD DETAILS
  - EC Quiescence Models
  - Knockdown and Overexpression Strategies
  - Transcriptomic Analysis
  - RNA Isolation and Quantitative RT-PCR
  - Immunoblot Analysis
  - Flow Cytometry Analysis
  - Metabolic Assays
  - ^{13}C Tracer Experiments and Metabolite Levels
  - In Vitro Functional Assays
  - Analysis of ROS Species
  - Immunochemistry and Morphometry
  - PCR Chromatin Immunoprecipitation
  - Luciferase Reporter Assay
  - Mouse Studies
  - Human Tissue Analysis
- QUANTIFICATION AND STATISTICAL ANALYSIS
- DATA AND SOFTWARE AVAILABILITY
  - Data Resources
  - Software

SUPPLEMENTAL INFORMATION

Supplemental Information includes seven figures and eight tables and can be found with this article online at https://doi.org/10.1016/j.cmet.2018.07.016.

ACKNOWLEDGMENTS

We thank R. Adams for providing Cdh5(PAC)-Cre^{ERT2} mice, S. Christen for help with GC-MS data interpretation, P. Levêque for help with EPR experiments and data interpretation, and the lab members for their assistance, feedback, and discussion. J.K., R.M., N.V.C., J.G., P.d.Z., F.M.-R., C.D., and U.H. are supported by the Research Foundation Flanders (FWO); L.B. by a Leopoldina Postdoc Scholarship; L.T. by a Marie Curie-IEF Fellowship; and L.-C.C. by Fritz Thyssen Stiftung. The work of R.C. is supported by a British Heart Foundation Intermediate Clinical Fellowship (FS/12/80/29821); S.J. is supported by Swiss National Science Foundation (BSCGI0_157859), Switzerland; S.-M.F. is supported by Marie Curie CIG, grants from the Research Foundation Flanders (FWO-Vlaanderen), Belgium; P.C. is supported by the VIB Tech-Watch program, a Federal Government Belgium grant (IUAP7/03), long-term structural Methusalem funding by the Flemish Government, grants from the Research Foundation Flanders (FWO-Vlaanderen), grants from Foundation against Cancer (2012-175 and 2016-078), and ERC Advanced Research grant (EU-ERC743074). X.L. is supported by the State Key Laboratory of Ophthalmology, Zhongshan Ophthalmic Center at the Sun Yat-Sen University and by the National Natural Science Foundation of China (81330021, 81670855).

AUTHOR CONTRIBUTIONS

J.K., L.B., N.V.C., R.M., I.E., U.B., S. Scheinok, L.T., A.R.C., C.D., P.d.Z., J.G., A.Z., F.T., F.M.-R., A.B., L.-C.C., S. Schoors, U.H., K.V., G.-A.P., R. Chen, R. Cubbon, B.T., B.C., B.W.W., B. Ghesquière, M.D., X.S., S.J., E.A.V.J., B. Gallez, D.L., M.M., G.E., X.L., S.-M.F., and P.C. contributed to the research and/or data analysis. J.K., L.B., and P.C. designed the experiments. J.K., L.B., N.V.C., R.M., X.L., and P.C. contributed to the execution, support, and analysis of experiments, data interpretation, and/or advice (with input of other co-authors). J.K and P.C. and wrote the paper. P.C. conceptualized and directed the study. All authors discussed the results and commented on the manuscript.

DECLARATION OF INTEREST

P.C. is named as inventor on patent applications claiming subject matter related to the results described in this paper. The other authors declare no competing interests.

Received: August 14, 2017
Revised: June 9, 2018
Accepted: July 28, 2018
Published: August 23, 2018

REFERENCES

Belousov, V.V., Fradkov, A.F., Lukyanov, K.A., Staroverov, D.B., Shakhbazov, K.S., Terskikh, A.V., and Lukyanov, S. (2006). Genetically encoded fluorescent indicator for intracellular hydrogen peroxide. Nat. Methods *3*, 281–286.

Benedito, R., Roca, C., Sorensen, I., Adams, S., Gossler, A., Fruttiger, M., and Adams, R.H. (2009). The notch ligands Dll4 and Jagged1 have opposing effects on angiogenesis. Cell *137*, 1124–1135.

Birben, E., Sahiner, U.M., Sackesen, C., Erzurum, S., and Kalayci, O. (2012). Oxidative stress and antioxidant defense. World Allergy Organ J. *5*, 9–19.

Cantelmo, A.R., Conradi, L.C., Brajic, A., Goveia, J., Kalucka, J., Pircher, A., Chaturvedi, P., Hol, J., Thienpont, B., Teuwen, L.A., et al. (2016). Inhibition of the glycolytic activator PFKFB3 in endothelium induces tumor vessel normalization, impairs metastasis, and improves chemotherapy. Cancer Cell *30*, 968–985.

Castel, D., Mourikis, P., Bartels, S.J., Brinkman, A.B., Tajbakhsh, S., and Stunnenberg, H.G. (2013). Dynamic binding of RBPJ is determined by Notch signaling status. Genes Dev. *27*, 1059–1071.

Chistiakov, D.A., Orekhov, A.N., and Bobryshev, Y.V. (2017). Effects of shear stress on endothelial cells: go with the flow. Acta Physiol. (Oxf) *219*, 382–408.

Christen, S., Lorendeau, D., Schmieder, R., Broekaert, D., Metzger, K., Veys, K., Elia, I., Buescher, J.M., Orth, M.F., Davidson, S.M., et al. (2016). Breast cancer-derived lung metastases show increased pyruvate carboxylase-dependent anaplerosis. Cell Rep. *17*, 837–848.

Cibor, D., Domagala-Rodacka, R., Rodacki, T., Jurczyszyn, A., Mach, T., and Owczarek, D. (2016). Endothelial dysfunction in inflammatory bowel diseases: pathogenesis, assessment and implications. World J. Gastroenterol. *22*, 1067–1077.

Dahlman, J.E., Barnes, C., Khan, O.F., Thiriot, A., Jhunjunwala, S., Shaw, T.E., Xing, Y., Sager, H.B., Sahay, G., Speciner, L., et al. (2014). In vivo endothelial siRNA delivery using polymeric nanoparticles with low molecular weight. Nat. Nanotechnol. *9*, 648–655.

Davidge, S.T. (2001). Prostaglandin H synthase and vascular function. Circ. Res. *89*, 650–660.

De Bock, K., Georgiadou, M., Schoors, S., Kuchnio, A., Wong, B.W., Cantelmo, A.R., Quaegebeur, A., Ghesquiere, B., Cauwenberghs, S., Eelen, G., et al. (2013). Role of PFKFB3-driven glycolysis in vessel sprouting. Cell *154*, 651–663.

Debacq-Chainiaux, F., Erusalimsky, J.D., Campisi, J., and Toussaint, O. (2009). Protocols to detect senescence-associated beta-galactosidase (SA-betagal) activity, a biomarker of senescent cells in culture and in vivo. Nat. Protoc. *4*, 1798–1806.

Donato, A.J., Morgan, R.G., Walker, A.E., and Lesniewski, L.A. (2015). Cellular and molecular biology of aging endothelial cells. J. Mol. Cell. Cardiol. *89*, 122–135.

Eelen, G., de Zeeuw, P., Treps, L., Harjes, U., Wong, B.W., and Carmeliet, P. (2018). Endothelial cell metabolism. Physiol. Rev. *98*, 3–58.

Egan, K., and FitzGerald, G.A. (2006). Eicosanoids and the vascular endothelium. Handb. Exp. Pharmacol. *176 Pt 1*, 189–211.

Fernandez, C.A., Des Rosiers, C., Previs, S.F., David, F., and Brunengraber, H. (1996). Correction of ^{13}C mass isotopomer distributions for natural stable isotope abundance. J. Mass Spectrom. *31*, 255–262.

Furuhashi, M., Saitoh, S., Shimamoto, K., and Miura, T. (2014). Fatty acid-binding protein 4 (FABP4): pathophysiological insights and potent clinical biomarker of metabolic and cardiovascular diseases. Clin. Med. Insights Cardiol. *8*, 23–33.

Ghesquiere, B., Wong, B.W., Kuchnio, A., and Carmeliet, P. (2014). Metabolism of stromal and immune cells in health and disease. Nature *511*, 167–176.

Gorrini, C., Harris, I.S., and Mak, T.W. (2013). Modulation of oxidative stress as an anticancer strategy. Nat. Rev. Drug Discov. *12*, 931–947.

Harjes, U., Bridges, E., Gharpure, K.M., Roxanis, I., Sheldon, H., Miranda, F., Mangala, L.S., Pradeep, S., Lopez-Berestein, G., Ahmed, A., et al. (2017). Antiangiogenic and tumour inhibitory effects of downregulating tumour endothelial FABP4. Oncogene *36*, 912–921.

Harjes, U., Bridges, E., McIntyre, A., Fielding, B.A., and Harris, A.L. (2014). Fatty acid-binding protein 4, a point of convergence for angiogenic and metabolic signaling pathways in endothelial cells. J. Biol. Chem. *289*, 23168–23176.

Harjes, U., Kalucka, J., and Carmeliet, P. (2016). Targeting fatty acid metabolism in cancer and endothelial cells. Crit. Rev. Oncol. Hematol. *97*, 15–21.

Harrington, L.S., Sainson, R.C., Williams, C.K., Taylor, J.M., Shi, W., Li, J.L., and Harris, A.L. (2008). Regulation of multiple angiogenic pathways by Dll4 and Notch in human umbilical vein endothelial cells. Microvasc. Res. *75*, 144–154.

Heiss, C., Rodriguez-Mateos, A., and Kelm, M. (2015). Central role of eNOS in the maintenance of endothelial homeostasis. Antioxid. Redox Signal. *22*, 1230–1242.

Huang, H., Vandekeere, S., Kalucka, J., Bierhansl, L., Zecchin, A., Bruning, U., Visnagri, A., Yuldasheva, N., Goveia, J., Cruys, B., et al. (2017). Role of glutamine and interlinked asparagine metabolism in vessel formation. EMBO J. *36*, 2334–2352.

Incalza, M.A., D'Oria, R., Natalicchio, A., Perrini, S., Laviola, L., and Giorgino, F. (2018). Oxidative stress and reactive oxygen species in endothelial dysfunction associated with cardiovascular and metabolic diseases. Vascul. Pharmacol. *100*, 1–19.

Kevil, C.G., Oshima, T., Alexander, B., Coe, L.L., and Alexander, J.S. (2000). H(2)O(2)-mediated permeability: role of MAPK and occludin. Am. J. Physiol. Cell Physiol. *279*, C21–C30.

Kratzer, E., Tian, Y., Sarich, N., Wu, T., Meliton, A., Leff, A., and Birukova, A.A. (2012). Oxidative stress contributes to lung injury and barrier dysfunction via microtubule destabilization. Am. J. Respir. Cell Mol. Biol. *47*, 688–697.

Lin, K., Hsu, P.P., Chen, B.P., Yuan, S., Usami, S., Shyy, J.Y., Li, Y.S., and Chien, S. (2000). Molecular mechanism of endothelial growth arrest by laminar shear stress. Proc. Natl. Acad. Sci. USA *97*, 9385–9389.

Nath, A., and Chan, C. (2016). Genetic alterations in fatty acid transport and metabolism genes are associated with metastatic progression and poor prognosis of human cancers. Sci. Rep. *6*, 18669.

Noseda, M., Chang, L., McLean, G., Grim, J.E., Clurman, B.E., Smith, L.L., and Karsan, A. (2004). Notch activation induces endothelial cell cycle arrest and participates in contact inhibition: role of p21Cip1 repression. Mol. Cell Biol. *24*, 8813–8822.

Oshitani, N., Kitano, A., Okabe, H., Nakamura, S., Matsumoto, T., and Kobayashi, K. (1993). Location of superoxide anion generation in human colonic mucosa obtained by biopsy. Gut *34*, 936–938.

Pascual, G., Avgustinova, A., Mejetta, S., Martin, M., Castellanos, A., Attolini, C.S., Berenguer, A., Prats, N., Toll, A., Hueto, J.A., et al. (2017). Targeting metastasis-initiating cells through the fatty acid receptor CD36. Nature *541*, 41–45.

Patella, F., Schug, Z.T., Persi, E., Neilson, L.J., Erami, Z., Avanzato, D., Maione, F., Hernandez-Fernaud, J.R., Mackay, G., Zheng, L., et al. (2015). Proteomics-based metabolic modeling reveals that fatty acid oxidation (FAO) controls endothelial cell (EC) permeability. Mol. Cell Proteomics *14*, 621–634.

Polet, F., and Feron, O. (2013). Endothelial cell metabolism and tumour angiogenesis: glucose and glutamine as essential fuels and lactate as the driving force. J. Intern. Med. *273*, 156–165.

Qu, Q., Zeng, F., Liu, X., Wang, Q.J., and Deng, F. (2016). Fatty acid oxidation and carnitine palmitoyltransferase I: emerging therapeutic targets in cancer. Cell Death Dis. *7*, e2226.

Rohrig, F., and Schulze, A. (2016). The multifaceted roles of fatty acid synthesis in cancer. Nat. Rev. Cancer *16*, 732–749.

Rostama, B., Turner, J.E., Seavey, G.T., Norton, C.R., Gridley, T., Vary, C.P., and Liaw, L. (2015). DLL4/Notch1 and BMP9 interdependent signaling induces human endothelial cell quiescence via P27KIP1 and thrombospondin-1. Arterioscler. Thromb. Vasc. Biol. *35*, 2626–2637.

Ruiz-Ramirez, A., Ortiz-Balderas, E., Cardozo-Saldana, G., Diaz-Diaz, E., and El-Hafidi, M. (2014). Glycine restores glutathione and protects against oxidative stress in vascular tissue from sucrose-fed rats. Clin. Sci. (Lond) *126*, 19–29.

Schieber, M., and Chandel, N.S. (2014). ROS function in redox signaling and oxidative stress. Curr. Biol. *24*, R453–R462.

Schoors, S., Bruning, U., Missiaen, R., Queiroz, K.C., Borgers, G., Elia, I., Zecchin, A., Cantelmo, A.R., Christen, S., Goveia, J., et al. (2015). Fatty acid carbon is essential for dNTP synthesis in endothelial cells. Nature *520*, 192–197.

Smolkova, K., and Jezek, P. (2012). The role of mitochondrial NADPH-dependent isocitrate dehydrogenase in cancer cells. Int. J. Cell Biol. *2012*, 273947.

Stoll, E.A., Makin, R., Sweet, I.R., Trevelyan, A.J., Miwa, S., Horner, P.J., and Turnbull, D.M. (2015). Neural stem cells in the adult subventricular zone oxidize fatty acids to produce energy and support neurogenic activity. Stem Cells *33*, 2306–2319.

Sumiyoshi, K., Mokuno, H., Iesaki, T., Shimada, K., Miyazaki, T., Kume, A., Kiyanagi, T., Kuremoto, K., Watanabe, Y., Tada, N., et al. (2008). Deletion of the Fc receptors gamma chain preserves endothelial function affected by hypercholesterolaemia in mice fed on a high-fat diet. Cardiovasc. Res. *80*, 463–470.

Tian, T., Wang, Z., and Zhang, J. (2017). Pathomechanisms of oxidative stress in inflammatory bowel disease and potential antioxidant therapies. Oxid. Med. Cell. Longev. *2017*, 4535194.

Ulrich, C.M., Steindorf, K., and Berger, N.A. (2013). Exercise, Energy Balance, and Cancer (Springer).

Wilhelm, K., Happel, K., Eelen, G., Schoors, S., Oellerich, M.F., Lim, R., Zimmermann, B., Aspalter, I.M., Franco, C.A., Boettger, T., et al. (2016). FOXO1 couples metabolic activity and growth state in the vascular endothelium. Nature *529*, 216–220.

Wong, B.W., Wang, X., Zecchin, A., Thienpont, B., Cornelissen, I., Kalucka, J., Garcia-Caballero, M., Missiaen, R., Huang, H., Bruning, U., et al. (2017). The role of fatty acid beta-oxidation in lymphangiogenesis. Nature *542*, 49–54.

Xiong, J., Kawagishi, H., Yan, Y., Liu, J., Wells, Q.S., Edmunds, L.R., Fergusson, M.M., Yu, Z.X., Rovira, I.I., Brittain, E.L., et al. (2018). A metabolic basis for endothelial-to-mesenchymal transition. Mol. Cell *69*, 689–698 e87.

STAR★METHODS

KEY RESOURCES TABLE

REAGENT or RESOURCE	SOURCE	IDENTIFIER
Antibodies		
Anti-Mouse IgG, HRP-linked	Cell Signaling Technology	7076S; RRID:AB_330924
Anti-Rabbit IgG, HRP-linked	Cell Signaling Technology	7074S; RRID:AB_2099233
Donkey anti-Goat IgG	Jackson ImmunoResearch	705-065-003; RRID:AB_2340396
Donkey anti-Mouse IgG	Jackson ImmunoResearch	715-065-151; RRID:AB_2340785
Donkey anti-Rabbit IgG	Jackson ImmunoResearch	711-065-152; RRID:AB_2340593
Donkey anti-Rat IgG	Jackson ImmunoResearch	712-065-153; RRID:AB_2315779
Goat anti-CD105	R&D Systems	AF1320; RRID:AB_354735
Goat anti-Rabbit IgG, Alexa Fluor 568	Thermo Fisher Scientific	A-11036; RRID:AB_10563566
Goat anti-Rabbit IgG, Alexa Fluor 647	Thermo Fisher Scientific	A-21245; RRID:AB_2535813
Human-anti-CD102-APC	Miltenyi Biotec	130-112-030; RRID:AB_2654351
Mouse anti-CD31	Dako, Agilent	M0823; RRID:AB_2114471
Mouse anti-PCNA	Leica Biosystems	NCL-L-PCNA; RRID:AB_2315078
Mouse anti-V5 tag	Thermo Fisher Scientific	R960-25; RRID:AB_2556564
Mouse anti-α-Tubulin	Sigma-Aldrich	T6074-100UL; RRID:AB_477582
Rabbit anti-acetyllysine	PTM-BioLab	PTM-105; RRID:N/A
Rabbit anti-Cleaved Notch1 (NICD)	Cell Signaling Technology	4147S; RRID: AB_2153348
Rabbit anti-CPT1A	Cell Signaling Technology	12252S; RRID:N/A
Rabbit anti-CPT1A	Proteintech	15184-1-AP; RRID:AB_2084676
Rabbit anti-PFKFB3	Cell Signaling Technology	13123S; RRID:AB_2617178
Rabbit anti-Phospho-AMPKα Thr172	Cell Signaling Technology	2531S; RRID:AB_330330
Rabbit anti-Total AMPKα	Cell Signaling Technology	2532S; RRID:AB_330331
Rabbit anti-VE-cadherin	Thermo Fisher Scientific	PA5-19612; RRID:AB_10979589
Rat anti-CD45	BD Pharmingen	553076; RRID:AB_394606
Rat anti-CD45-PeCy7	Thermo Fisher Scientific	25-0451-82; RRID:AB_469625
Rat anti-Notch1	Cell Signaling Technology	3447S; RRID:AB_2153498
Biological Samples		
Human blood samples (-Ethics Committee Research UZ/KU Leuven approval number S57736)	This paper	N/A
Chemicals, Peptides, and Recombinant Proteins		
[1-^{14}C]D-glucose	Hartmann Analytic	ARC 0120A
[5-^{3}H]D-glucose	Perkin Elmer	NET531001MC
[6-^{14}C]D-glucose	Perkin Elmer	NEC045X050UC
[6-^{14}C]D-glucose	Hartmann Analytic	ARC 0121A
[6-^{3}H]thymidine	Perkin Elmer	NET355L005MC
[9,10-^{3}H]palmitic acid	Perkin Elmer	NET043001MC
[U-^{13}C]D-glucose	Cambridge isotope laboratories	CLM-1396
[U-^{13}C]-L-glutamine	Cambridge isotope laboratories	CLM-1166
[U-^{13}C]potassium palmitate	Cambridge isotope laboratories	CLM-3943
[U-^{13}C]sodium acetate	Sigma-Aldrich	282014
[U-^{14}C]acetate	Perkin Elmer	NEC553050UC
[U-^{14}C]glutamine	Perkin Elmer	NEC451050UC
[U-^{14}C]palmitic acid	Perkin Elmer	NEC534050UC
1-[2,3,4-trimethoxybenzyl]piperazine dihydrochloride (TMZ)	Sigma-Aldrich	653322
5-ethynyl-2'-deoxyuridine (EdU)	Thermo Fisher Scientific	A10044

(*Continued on next page*)

Continued

REAGENT or RESOURCE	SOURCE	IDENTIFIER
Alexa-488 Fluor conjugated phalloidin	Thermo Fisher Scientific	A12379
Alexa-647 Fluor conjugated isolectin B4	Thermo Fisher Scientific	I32450
Calcein	Thermo Fisher Scientific	C1430
CM-H_2DCFDA	Thermo Fisher Scientific	C6827
CPT1A inhibitor (+)-etomoxir sodium salt hydrate (2-[6-(4-chlorophenoxy)hexyl]oxirane-2-carboxylate	WuXi AppTec	N/A
Delta like ligand 4 (rhDll4)	R&D Systems	1506-D4-050/CF
Dextran sulfate sodium (DSS) 36,000-50,000 M.Wt.	MP Biomedicals	0216011010
Dextran, Tetramethylrhodamine, 70,000 MW, Lysine Fixable	Thermo Fisher Scientific	D1818
DHE (dihydroethidium)	Thermo Fisher Scientific	D1168
dNTP Set (100 mM)	Thermo Fisher Scientific	10297018
eBioscience Fixable Viability Dye eFluor 450	Thermo Fisher Scientific	65-0863-14
Ficoll-paque plus	GE Healthcare	17144002
Hoechst 33342	Thermo Fisher Scientific	H3570
Potassium hydroxycitrate tribasic monohydrate	Sigma-Aldrich	59847
L-carnitine	Sigma-Aldrich	C0283
L-glutamine	Thermo Fisher Scientific	25030024
Lipopolysaccharides from *Escherichia coli* 0111:B4	Sigma-Aldrich	L2630-100MG
MitoSOX Red	Thermo Fisher Scientific	M36008
mitoTEMPO	Sigma-Aldrich	SML0737
Oligo(dT)20 Primer	Thermo Fisher Scientific	18418020
Oligomycin	Sigma-Aldrich	O4876
Phosphatase inhibitors (PhosSTOP)	Roche	04906837001
Protease inhibitors (cOmplete, EDTA-free Protease Inhibitor Cocktail)	Roche	11873580001
Proteinase K	Thermo Fisher Scientific	25530049
RNase A	Thermo Fisher Scientific	EN0531
RNaseOUT Recombinant Ribonuclease Inhibitor	Thermo Fisher Scientific	10777019
Sodium acetate	Sigma-Aldrich	S2889
Sodium palmitate	Sigma-Aldrich	P9767
Sodium pyruvate	Thermo Fisher Scientific	11360070
Tamoxifen	Sigma-Aldrich	T5648
Trichloroacetic acid (TCA)	Sigma-Aldrich	T6399
X-Gal (5-bromo-4-chloro-3-indolyl-β-D-galactoside)	Thermo Fisher Scientific	15520034
γ-secretase inhibitor DAPT (N-[N-(3,5-Difluorophenacetyl)-L-alanyl]-S-phenylglycine t-butyl ester)	Sigma-Aldrich	D5942
Critical Commercial Assays		
Acetyl-Histone Antibody Sampler Kit	Cell Signaling Technology	9933T
Agencourt AMPure XP	Beckman Coulter	A63880
Amplex Red Hydrogen Peroxide/Peroxidase Assay Kit	Thermo Fisher Scientific	A22118
ATPlite	Perkin Elmer	6016943
CD31 MicroBead Kit, human	Miltenyi Biotec	130-091-935
CD31 MicroBeads, mouse	Miltenyi Biotec	130-097-418
CD45 MicroBeads, mouse	Miltenyi Biotec	130-052-301
Click-iT EdU Alexa Fluor 488 Imaging Kit	Thermo Fisher Scientific	C10337
Click-iT EdU Alexa Fluor 647 Imaging Kit	Thermo Fisher Scientific	C10340
Cytotoxicity Detection Kit^{PLUS} (LDH)	Roche	04744934001
Dual Luciferase Reporter Kit	Promega	E1910

(*Continued on next page*)

Continued

REAGENT or RESOURCE	SOURCE	IDENTIFIER
Illumina TotalPrep RNA Amplification Kit	Thermo Fisher Scientific	AMIL1791
iScript cDNA synthesis kit	Bio-Rad	1708891
Lung Dissociation Kit, mouse	Miltenyi Biotec	130-095-927
MACSPlex Cytokine Kit (mouse)	Miltenyi Biotec	130-101-740
Nucleofector Kits for Human Umbilical Vein Endothelial Cells (HUVEC)	Lonza	VPB-1002
Pierce Protein A/G Magnetic Beads	Thermo Fisher Scientific	88802
Pierce ECL Western Blotting Substrate	Thermo Fisher Scientific	32106
PowerUp SYBR Green Master Mix	Thermo Fisher Scientific	A25742
PureLink RNA Mini Kit	Thermo Fisher Scientific	12183018A
SuperScript III Reverse Transcriptase	Thermo Fisher Scientific	18080044
SuperSignal West Femto Maximum Sensitivity Substrate	Thermo Fisher Scientific	34095
TaqMan Fast Universal PCR Master Mix (2X), no AmpErase UNG	Thermo Fisher Scientific	4364103
TSA Cyanine 3 (Cy3) System	Perkin Elmer	NEL704A001KT
TSA Cyanine 5 (Cy5) System	Perkin Elmer	NEL705A001KT
TSA Fluorescein System	Perkin Elmer	NEL701A001KT
Deposited Data		
Microarray raw and analyzed data	This paper	GEO: GSE89174
RNA-sequencing raw and analyzed data	This paper	ArrayExpress: E-MTAB-6595
Experimental Models: Cell Lines		
293T cells	ATCC	CRL-3216
Human umbilical artery endothelial cells (HUAECs); Approved by Ethics Committee Research UZ/KU Leuven; approval number S57123	This paper	N/A
Human umbilical vein endothelial cells (HUVECs); Approved by Ethics Committee Research UZ/KU Leuven; approval number S57123	This paper	N/A
Mouse endothelial cells; Approved by the Institutional Animal Ethics Committee of the KU Leuven	This paper	N/A
Experimental Models: Organisms/Strains		
Mouse: CPT1A$^{lox/lox}$ C57BL/6	Schoors et al., 2015	N/A
Mouse: Cre-driver line Cdh5(PAC)-Cre^{ERT2} C57BL/6	Benedito et al., 2009	N/A
Oligonucleotides		
ChiP-qPCR primers (Table S8)	IDT	N/A
qRT-PCR primers (Table S8)	IDT	N/A
shRNA oligonucleotides (Table S8)	Sigma-Aldrich Schoors et al., 2015	N/A
Recombinant DNA		
pGL3 basic luciferase plasmid	Promega	E1751
pHyPer-dMito vector	Evrogen	FP942
pLKO-shRNA2 vector	Clontech	No. PT4052-5
pRRLsinPPT.CMV.MCS MM WPRE vector	Wong et al., 2017	N/A
V5 tagged murine Notch1 NICD cDNA	Gift from M. Potente	N/A
Software and Algorithms		
Adobe Illustrator CC	Adobe Systems Incorporated	https://www.adobe.com/be_en/products/illustrator.html
D3heatmap package	Cantelmo et al., 2016	N/A
EdgeR package	Cantelmo et al., 2016	N/A
Fiji (Image J)	Open Source	https://fiji.sc
FlowJo 8.8.6 software	FlowJo, LLC	https://www.flowjo.com

(*Continued on next page*)

Continued

REAGENT or RESOURCE	SOURCE	IDENTIFIER
Prism v.6 software	Graphpad	http://www.graphpad.com
Leica MM AF powered by MetaMorph analysis software	Leica microsystems	N/A
limma package	Cantelmo et al., 2016	N/A
Pathview package	Cantelmo et al., 2016	N/A
Pvclust package	Cantelmo et al., 2016	N/A
RStudio	Open Source	https://www.rstudio.com
Xcalibur Software	Thermo Fisher Scientific	N/A
Other		
16% Formaldehyde (w/v), Methanol-free	Thermo Fisher Scientific	28906
6.5 mm Transwell with 0.4 μm Pore Polyester Membrane Insert	Corning	3470
Antibiotic-Antimycotic (100X)	Thermo Fisher Scientific	15240062
Bovine Serum Albumin	Sigma-Aldrich	A8806
CAT-peg	Sigma-Aldrich	C4963
Cell lysis buffer (10x)	Cell Signaling Technology	9803
Collagenase I	Thermo Fisher Scientific	17100017
Collagenase I	Sigma-Aldrich	C0130
Collagenase II	Thermo Fisher Scientific	17101015
Collagenase IV	Worthington Biochemical Corporation	LS004188
Corning 100μm Cell Strainer	Corning	431752
DIPPMPO	Enzo Life Science	ALX-430-119-M050
Dispase II	Thermo Fisher Scientific	17105041
DNase I	Sigma-Aldrich	D4527
DTPA	Sigma-Aldrich	D6518
Dulbecco's phosphate-buffered saline (DPBS)	Thermo Fisher Scientific	14190144
Dulbecco's Modified Eagle medium	Thermo Fisher Scientific	41965047
EGM2 (Endothelial growth medium)	PromoCell	C-22011
Endothelial cell growth factor supplements (ECGS/ Heparin)	PromoCell	C-30120
Endothelial Cell Growth Medium 2 SupplementMix	PromoCell	C-39216
Falcon 70 μm Cell Strainer	Corning	352350
FBS (Fetal Bovine Serum)	Biochrom BmgH	S0115
FBS (Fetal Bovine Serum), charcoal stripped	Sigma-Aldrich	F6765
Gelatin from bovine skin	Sigma-Aldrich	G9391
Hydrogen peroxide 30%	Merck, Millipore	8222871000
IGEPAL CA-630	Sigma-Aldrich	I8896
Ketamine 100 mg/mL	NIMATEK	N/A
Medium 199 (M199), HEPES	Thermo Fisher Scientific	22340020
MEM Non-Essential Amino Acids Solution	Thermo Fisher Scientific	11140050
Nitrocellulose Pre-Cut Blotting Membranes, 0.45 μm pore size	Thermo Fisher Scientific	LC2001
NuPAGE 10% Bis-Tris Protein Gels, 1.5 mm, 10-well	Thermo Fisher Scientific	NP0315BOX
NuPAGE 4-12% Bis-Tris Protein Gels, 1.5 mm, 10-well	Thermo Fisher Scientific	NP0335BOX
NuPAGE LDS Sample Buffer (4X)	Thermo Fisher Scientific	NP0007
NuPAGE MES SDS Running Buffer (20X)	Thermo Fisher Scientific	NP0002
NuPAGE MOPS SDS Running Buffer (20X)	Thermo Fisher Scientific	NP0001
NuPAGE Sample Reducing Agent (10X)	Thermo Fisher Scientific	NP0009
NuPAGE Transfer Buffer (20X)	Thermo Fisher Scientific	NP00061
Penicillin/streptomycin	Thermo Fisher Scientific	15140122
PVDF Pre-cut Blotting Membranes, 0.2 μm pore size	Thermo Fisher Scientific	LC2002
SOD-peg	Sigma-Aldrich	S9549

(*Continued on next page*)

Continued

REAGENT or RESOURCE	SOURCE	IDENTIFIER
Sodium butyrate	Sigma-Aldrich	303410
SuperFrost Excell object slides	Thermo Scientific Menzel	J5800AMNZ
TE (Tris-EDTA) buffer	Thermo Fisher Scientific	12090015
Trichostatin A (TSA)	Sigma-Aldrich	T8552
TRIzol LS reagent	Thermo Fisher Scientific	10296028
Trypsin-EDTA (0.25%)	Thermo Fisher Scientific	25200056
XYL-M2%	Livestock Pharma	BEV170581

CONTACT FOR REAGENT AND RESOURCE SHARING

Further information and requests for resources and reagents should be directed to and will be fulfilled by the Lead Contact, Peter Carmeliet (peter.carmeliet@kuleuven.vib.be).

EXPERIMENTAL MODEL AND SUBJECT DETAILS

Mice

Animal housing and all experimental procedures were approved by the Institutional Animal Ethics Committee of the KU Leuven (Belgium). Mice from the EC-specific inducible Cre-driver line Cdh5(PAC)-Cre^{ERT2} (Benedito et al., 2009) were crossed with previously generated *Cpt1a*$^{lox/lox}$ mice (Schoors et al., 2015) to obtain mice with EC-specific deletion of the *Cpt1a* gene upon tamoxifen treatment to induce Cre-mediated gene excision (CPT1A$^{\Delta EC}$ mice). These lines were on a 100% C57BL/6 background. Tamoxifen (Sigma-Aldrich) treatment was done using 8-week-old mice by gavage (0.114 mg/g body weight/day, for 5 consecutive days and an additional day after a 2-day treatment free interval) one week before the experiment.

Cell Isolation and Culture

Primary Human Umbilical Endothelial Cells

Human umbilical vein endothelial cells (HUVECs) and human umbilical artery endothelial cells (HUAECs) were freshly isolated from umbilical cords obtained from multiple donors (with approval from the Ethics Committee Research UZ/KU Leuven and informed consent obtained from all subjects) as previously described (Schoors et al., 2015), regularly tested for mycoplasma. The ECs were maintained in M199 medium (1 mg/mL D-glucose) (Thermo Fisher Scientific) supplemented with 20% fetal bovine serum (FBS) (Biochrom BmgH), 2 mM L-glutamine (Thermo Fisher Scientific), Endothelial Cell Growth Supplement (ECGS)/ Heparin (PromoCell), 100 IU/mL penicillin and 100 μg/mL streptomycin (Thermo Fisher Scientific) or in endothelial cell basal medium (EGM2) (PromoCell) supplemented with endothelial cell growth medium supplement pack (PromoCell). In all experiments, HUVECs and HUAECs were always used as single-donor cultures and were used between passage (p) 1 and 4.

Adult Human Endothelial Cells

As a source of adult human ECs, we used ECs isolated from healthy adjacent tissue from lung or kidney tumor biopsies. Following surgical resection, adjacent lung or kidney tissue was taken, and transported to the research facility (with approval from the Medical Ethical Committee KU Leuven/UZ Leuven). Upon arrival, samples were rinsed with PBS (Thermo Fisher Scientific), minced into smaller pieces of less than 1 mm^3, and transferred to 5 mL digestion medium consisting of Dulbecco's Modified Eagle medium (DMEM) (4500 mg/L glucose) (Thermo Fisher Scientific), supplemented with 100 U/mL penicillin/streptomycin (Thermo Fisher Scientific), 1 mM sodium pyruvate (Thermo Fisher Scientific), MEM NEAAs (1x) (Thermo Fisher Scientific), 2 mM glutamine (ThermoFisher Scientific), endothelial cell growth medium supplement pack (PromoCell) and containing 0.2% collagenase I/II (Thermo Fisher Scientific), 250 μg/mL DNase (Sigma-Aldrich) and 0.25 U/mL Dispase (Thermo Fisher Scientific). Samples were incubated for 30 min at 37°C, with manual shaking every 5 min. Next, 10 mL cold PBS containing BSA 0.1% (Sigma-Aldrich) were added and the samples were filtered using a 100 μm strainer (Corning, NY, USA). Following centrifugation at 300 g at RT for 5 min, the supernatant was decanted and discarded. The cell pellet was resuspended in 6 mL of a mix of M199 (containing 10% FBS and sodium pyruvate, MEM NEAAs, glutamine and heparin as above) and EGM2 medium (1:1), further supplemented with antibiotic/antimycotic (2x) (Thermo Fisher Scientific). The single cell suspension was plated out in 3 wells of a 6-well plate pre-coated with 0.1% gelatin (Sigma-Aldrich). The next day the medium was changed to EGM2 supplemented with antibiotic/antimycotic (Thermo Fisher Scientific) and thereafter refreshed every other day. When reaching confluency and upon detection of EC cell colonies (patches with cobblestone appearance), the ECs were purified using human anti-CD31 coated magnetic beads according to the manufacturer's instructions (MACS Technology, Miltenyi Biotec). The resulting MACS-purified endothelial cells were further cultured in EGM2 medium as single-donor cultures and used for experiments in as early passage as possible (usually up to passage 3-5).

Adult Mouse Endothelial Cells

Mouse ECs were isolated from perfused healthy lungs of adult CPT1A$^{\Delta EC}$ mice and their WT littermates. Briefly, before starting the perfusion, the mice were anesthetized with Ketamine/Xylazine (500 μL/mouse of Ketamine 0.65%; Xylazine 0.05% diluted in

physiologic saline solution) and once the withdrawal reflex was absent in pelvic limbs, the perfusion procedure was started. Mice were perfused with 5 mL of PBS followed by dissection and dissociation of the lung using the Lung Dissociation Kit according to the manufacturer's instructions (Miltenyi Biotec), at a perfusion rate of 2 mL/min. Lungs were further dissociated using the gentleMACS dissociator system (MACS Technology, Miltenyi Biotec). Next, samples were centrifuged, resuspended in 5 mL of PBS based wash buffer (containing 0.5% BSA; 2 mM EDTA) and applied to a pre-separation 70 μm filter (Corning, NY, USA). The filtered cells were washed twice with wash buffer and ECs were selected using first CD45 MicroBeads to deplete $CD45^+$ cells and then labelled with CD31 MicroBeads according to the manufacturer's instructions (MACS Technology, Miltenyi Biotec). Positively selected $CD31^+$ cells were stained with viability dye, CD102-APC and CD45-PeCy7 and the fraction of viable, $CD102^+$ and $CD45^-$ cells obtained by FACS sorting was directly collected into TRIzol LS reagent (Thermo Fisher Scientific).

Neonatal Mouse (P8) Endothelial Cells

ECs were isolated from perfused lungs, hearts, and livers of P8 mice treated with etomoxir (30 mg/kg; i.p. injection once a day starting 48 hr before euthanization) or vehicle (0.9% NaCl). To obtain a sufficient number of ECs, organs of three P8 mice of each group were pooled. For detection of proliferating cells, 5-ethynyl-2'-deoxyuridine (EdU) (Thermo Fisher Scientific) was injected 2 hr before organ dissection. As described above, mice were anesthetized with Ketamine/Xylazine and the perfusion procedure was started once the withdrawal reflex was absent in pelvic limbs. Mice were perfused with 1 mL of PBS followed by dissection and dissociated with 5 mL of a DMEM based digestion buffer containing either 0.2% collagenase II, 0.2% collagenase IV (lungs, hearts) or 0.1% collagenase I, 0.1% collagenase II (livers), Dispase (0.25 U/mL) (livers and hearts) (Thermo Fisher Scientific), 250 μg/mL DNase (Sigma-Aldrich), 2 mM $CaCl_2$, 1% antibiotic/antimycotic, at a perfusion rate of 1 mL/minute. Lungs and hearts were further dissociated using the gentleMACS dissociator system (MACS Technology, Miltenyi Biotec). Next, samples were centrifuged, resuspended in 5 mL of PBS based wash buffer (containing 0.5% BSA; 2 mM EDTA) and applied to a pre-separation 70 μm filter (Corning, NY, USA). The filtered cells were washed twice with wash buffer and ECs were selected using CD45 MicroBeads to deplete CD45+ cells (this step was only applied to lung and heart tissue) and CD31 MicroBeads according to the manufacturer's instructions (MACS Technology, Miltenyi Biotec). Isolated cells were used immediately to assess ROS levels and cell cycle phase as described in detail below (See Flow Cytometry Analysis: Analysis Of Endothelial Superoxide Levels and Cell Cycle In Vivo).

METHOD DETAILS

EC Quiescence Models

Contact Inhibition Model of EC Quiescence

ECs (p1 or p2) were seeded in 100% EGM2 at a density of 15,000 cells/cm^2. During the progressive induction of EC-quiescence, the culture medium was gradually changed from 100% EGM2 to M199/EGM2 mix in ratio 1:1 (further referred to as growth medium). To generate the corresponding proliferative control, contact inhibited cells (day 6 QECs) were trypsinized (using Trypsin-EDTA (0.25%); Thermo Fisher Scientific) and cultured in growth medium for at least 36 hr to re-initiate proliferation. PECs, used as proliferating controls for contact-inhibited QECs are always reseeded QECs.

Dll4 Stimulation Model of EC Quiescence

Culture plates were coated overnight at 4°C on a plate shaker with 1 μg/mL recombinant human Delta like ligand4 (rhDll4, R&D Systems) with 0.1% gelatin. The control plates were coated with 0.1% gelatin supplemented with 0.02% BSA (Sigma-Aldrich), which was used as a carrier for Dll4. Prior to EC seeding, excessive coating solution was removed by aspiration and ECs were seeded at a density of 30,000 cells/cm^2 in growth medium. Experiments were performed 24 hr after seeding. PECs, used as proliferating controls for Dll4-induced QECs are always ECs grown in parallel on BSA coated plates.

Laminar Shear Stress Model of EC Quiescence

ECs were seeded at a density of 30,000 cells/cm^2 in growth medium on SuperFrost Excell object slides (Thermo Scientific Menzel) overnight and exposed to laminar shear stress (10 dynes/cm^2) for 24 hr. The parallel-plate flow chamber system was built in-house and combined with a peristaltic pump (COLE-PARMER INSTRUMENT 7519-06 Masterflex L/S Cartridge Pump Head, 8-Channel, 4-Roller). HUVECs seeded on SuperFrost object slides overnight were used as static controls.

Knockdown and Overexpression Strategies

Lentiviral Transductions

For overexpression of the Notch intracellular domain (V5-NICD; gift from M. Potente), the cDNA was cloned in the pRRLsinPPT.CMV.MCS MM W prevector (Wong et al., 2017). To generate shRNA vectors against *CPT1A*, *ACSS1*, *IDH2*, *ME3*, *ACADvl* and *HADHB* oligonucleotides were cloned into the pLKO-shRNA2 vector (Clontech). A nonsense scrambled shRNA sequence was used as a negative control. Oligonucleotides are listed in the Key Resources Table. Production of lentiviruses by transfection into 293T cells was performed as described (Wong et al., 2017). For transductions, a multiplicity of infection (MOI) of 5 was used for all shIDH2 experiments, 10 was used for all shME3, shACADvl and shHADHB experiments, 20 was used in all shCPT1A, shACSS1 experiments. For transductions with NICD, a MOI of 10 was used. Cells were transduced overnight and re-fed with fresh medium the next day. Transduced cells were used in functional assays at least 3 to 4 days post-transduction.

Transcriptomic Analysis

Microarray Analysis

RNA from PECs and contact-inhibited QECs was extracted, reverse transcribed into cDNA, biotin-UTP labelled using the Illumina TotalPrep RNA Amplification kit (Thermo Fisher Scientific) and hybridized to the Illumina HumanHT-12 v4 Expression BeadChip for micro-array analysis using standard protocols (Illumina). Differentially expressed genes and their false discovery rate (FDR) corrected p values were identified by the limma package (Cantelmo et al., 2016). Heatmap analysis was performed using the D3heatmap package, and significant clusters were calculated via multiscale bootstrap analysis with the Pvclust package (Cantelmo et al., 2016). The rotation gene set (ROAST) algorithm as implemented in the limma package was used to perform self-contained gene set analysis. Gene expression data were mapped on KEGG metabolic pathways using Pathview (Cantelmo et al., 2016). Microarray data are available in GEO (www.ncbi.nlm.nih.gov/geo/) under accession GSE89174.

RNA-sequencing

RNA from freshly isolated murine lung ECs was prepared using TRIzol reagent according to the manufacturer's instruction. Starting from 1 μg total RNA, poly-adenylated fragments were isolated, reverse transcribed, and converted into indexed sequencing libraries using the KAPA stranded mRNA-seq kit (Sopachem, Eke, Belgium). The first 50 bases of these libraries were sequenced on a HiSeq 4000 system (Illumina, San Diego, CA). The raw sequenced reads were mapped to the mouse reference transcriptome and genome (GRCm38/mm10) using the Bowtie TopHat pipeline. Mapped reads were assigned to Ensembl gene IDs by HTSeq, resulting in on average 14,814,487 ± 5,948,836 counts per sample. Genes expressed at a level of at least 1 count per million reads in at least three of eight samples were filtered out with the EdgeR package (Cantelmo et al., 2016), and differentially expressed genes and their false discovery rate (FDR) corrected p values were identified using Limma (Cantelmo et al., 2016). Heatmap analysis was performed using the D3heatmap package and significant clusters were calculated via multiscale bootstrap analysis with the Pvclust package (Cantelmo et al., 2016). The rotation gene set (ROAST) algorithm as implemented in the Limma package (Cantelmo et al., 2016) was used to perform self-contained gene set analysis. Gene expression data were mapped on KEGG metabolic pathways using Pathview. RNA-sequencing data are available in GEO (https://www.ncbi.nlm.nih.gov/geo/) under accession E-MTAB-6595.

RNA Isolation and Quantitative RT-PCR

RNA was collected and purified using the PureLink RNA Mini Kit (Thermo Fisher Scientific) and converted to cDNA using the iScript cDNA synthesis kit (Bio-Rad). For RNA-sequencing validation, RNA from isolated ECs was collected into TRIzol Reagent and extracted and, then, converted to cDNA using the SuperScript III Reverse Transcriptase (Thermo Fisher Scientific). RNA expression analysis was performed by Taqman quantitative RT-PCR (Thermo Fisher Scientific) as described using premade primer sets (IDT) (Schoors et al., 2015). Premade primer set ID numbers are listed in the Key Resources Table. For comparison of gene expression between conditions, expression (normalized to HPRT endogenous control) is expressed relative to control condition.

Immunoblot Analysis

Protein extraction and immunoblot analysis were performed using a modified Laemmli sample buffer (125 mM Tris-HCl, pH 6.8 buffer containing 2% SDS and 10% glycerol) or cell lysis buffer (Cell Signaling Technology) in the presence of protease and phosphatase inhibitors (Roche). Lysates were separated by SDS-PAGE under reducing conditions, transferred to a nitrocellulose or PVDF membrane, and analyzed by immunoblotting. Primary antibodies used were rabbit anti-CPT1A (Cell Signaling Technology), anti-total AMPKα (Cell Signaling Technology), rabbit anti-phospho-AMPKα Thr172 (Cell Signaling Technology), anti-PFKFB3 (Cell Signaling Technology), anti-NICD (Cell Signaling Technology), anti-Histone H2A (Cell Signaling Technology), anti-Acetyl-Histone H2A (Lys5) (Cell Signaling Technology), anti-Histone H3 (Cell Signaling Technology), anti-Acetyl-Histone H3 (Lys9) (Cell Signaling Technology), anti-Histone H4 (Cell Signaling Technology), anti-Acetyl-Histone H4 (Lys8) (Cell Signaling Technology), anti-α-tubulin (Sigma) and anti-acetyllysine (PTM-Biolab). Appropriate secondary antibodies were from Cell Signaling Technology. Signal was detected using the ECL or Femto system (Thermo Fisher Scientific) according to the manufacturer's instructions. Densitometric quantifications of bands were done with Fiji software (https://fiji.sc).

Histone Extraction

ECs were washed with cold PBS, scraped and collected in cold hypotonic lysis buffer (10 mM Tris-HCL (pH 7.5), 1 mM KCl, 1.5 mM $MgCl_2$, to which was freshly added: 1 mM DTT, 1× protease inhibitors, 10 mM sodium butyrate (Sigma-Aldrich), 0.1% IGEPAL (an NP-40 substitute; Sigma-Aldrich), 1 μM trichostatin A (TSA; Sigma-Aldrich). The collected samples were incubated for 30 min on a rotator at 4°C to promote hypotonic swelling of cells and lysis by mechanical shearing during rotation. Nuclei were pelleted at 15,000 rpm for 5 min at 4°C and immediately resuspended in 0.4 N H_2SO_4 followed by incubation overnight at 4°C. After centrifugation at 15,000 rpm for 10 min at 4°C, histones were precipitated from the supernatant by addition of 20% trichloroacetic acid for 2 hr, followed by centrifugation at 15,000 rpm for 10 min at 4°C. Pellets were washed twice with acetone. Histone proteins were resuspended in H_2O and used for immunoblot analysis.

Flow Cytometry Analysis

In Vivo Analysis of Endothelial Superoxide Levels and Cell Cycle

We developed a new FACS based method to measure ROS levels and subsequently proliferation of ECs freshly isolated from different organs (heart, liver, lung) of P8 neonatal mice, in which blood vessels are still growing and expanding (thus containing PECs) but also already contain QECs. Because of technical reasons, we first had to stain and sort for the ROS marker dehydroethidium (DHE) and

thereafter for EdU as described below. This avoided that when first stained for EdU, the DHE signal was completely lost due to the fixation and permeabilization treatment required for the EdU nuclear staining.

Detection of Superoxide Levels in Freshly Isolated Murine ECs. Briefly, freshly isolated Ecs from lungs, hearts, and livers of P8 neonatal mice (as described above) were stained with viability dye, CD45-PeCy7, CD102-APC and DHE (20 μmol/L; Thermo Fisher Scientific) at 4°C for 30 min. Next, based on DHE staining we FACS sorted viable, $CD45^-$, $CD102^+$ and DHE^+ ECs and viable, $CD45^-$, $CD102^+$ and DHE^- ECs separately into two Eppendorf tubes. The cells were then immediately processed and stained for EdU as described below.

Cell Cycle Analysis In Freshly Isolated Murine ECs. Cells in G1 were identified as a population positive for EdU incorporation. Briefly, the DHE^+ and DHE^- FACS sorted ECs from lungs, hearts, and livers of EdU treated P8 mice were fixed with 4% PFA (15 min at RT). The incorporated EdU was detected by a 'click-It reaction' with Alexa Fluor 488 according to the manufacturer's instructions (Thermo Fisher Scientific). Data were recorded by flow cytometry, and analyzed with the FlowJo 8.8.6 software (https://www.flowjo.com).

Cell Cycle Analysis In Vitro

Cells in G0 were identified as a 2N DNA population lacking EdU incorporation. Briefly, cells were labeled with 10 μM EdU over 24 hr, collected by trypsinization and fixed (4% PFA). The incorporated EdU was detected by a 'click-It reaction' with Alexa Fluor 647 according to the manufacturer's instructions (Thermo Fisher Scientific). Data were recorded by flow cytometry, and resultant data were analyzed with the FlowJo 8.8.6 software (https://www.flowjo.com).

Metabolic Assays

Fatty Acid Oxidation

ECs were incubated in fully supplemented growth medium, supplemented with 100 μM unlabeled palmitate and 50 μM carnitine (Sigma-Aldrich). Cells were incubated for 6 hr in growth medium containing 2 μCi/mL [9,10-^{3}H]palmitatic acid (Schoors et al., 2015; Wong et al., 2017) (Perkin Elmer). Thereafter, supernatant was transferred into glass vials sealed with rubber stoppers. ^3H_2O was captured in hanging wells containing a Whatman paper soaked with H_2O over a period of 48 hr at 37°C to reach saturation (Schoors et al., 2015). Radioactivity was determined by liquid scintillation counting.

Glycolysis

Glycolysis was measured analogously to fatty acid oxidation (see above) using 80 mCi/mmol [5-^{3}H]D-glucose (Perkin Elmer) (Schoors et al., 2015).

Fatty Acid Synthesis

ECs were incubated in growth medium supplemented with [U-^{14}C]acetate (Perkin Elmer) for 24 hr following snap freezing and methanol-water-chloroform extraction. Phase separation was achieved by centrifugation at 4°C and the methanol-water phase containing polar metabolites was used as negative control. Chloroform phase containing fatty acids was added to scintillation liquid and counts were normalized to protein concentrations determined of the dried protein interphase.

^{14}C-glucose Oxidation

Cells were incubated for 6 hr in growth medium containing 100 μCi/mmol [6-^{14}C]D-glucose (Perkin Elmer). Thereafter, 250 μL of 2 M perchloric acid was added to each well to stop cellular metabolism and wells were immediately covered with a 1x hyamine hydroxide-saturated Whatman paper. Overnight absorption of $^{14}CO_2$ released during oxidation of glucose into the paper was performed at room temperature, and radioactivity in the paper was determined by liquid scintillation counting.

^{14}C-glutamine Oxidation

^{14}C-glutamine Oxidation was performed similarly as glucose oxidation, except that 0.5 μCi/mL [U-^{14}C]glutamine (Perkin Elmer) as tracer was used.

Oxidative Pentose Phosphate Pathway

The oxidative pentose phosphate pathway (oxPPP) flux was measured as $^{14}CO_2$ formation using [6-^{14}C]D-glucose (Hartmann Analytic) ($^{14}CO_2$ formation only in the TCA cycle) and [1-^{14}C]D-glucose (Hartmann Analytic) ($^{14}CO_2$ formation in both the TCA cycle and the oxPPP). Cells were incubated in parallel in medium containing [6-^{14}C]D-glucose (1 μCi/mmol) or medium containing [1-^{14}C]D-glucose (1 μCi/mmol). Released $^{14}CO_2$ was captured in a similar manner as described above for the glucose or glutamine oxidation. The oxPPP flux was then calculated by subtracting the [6-^{14}C]D-glucose flux from the [1-^{14}C]D-glucose flux and was normalized to the glycolytic flux to correct for total cellular glucose usage.

Palmitate Mediated DNA, RNA and Protein Synthesis

Palmitate mediated DNA, RNA and protein synthesis was measured by the incorporation of ^{14}C into DNA, RNA or protein using 100 μCi/mmol [U-^{14}C]palmitic acid (Perkin Elmer) and was corrected for the total amount of DNA/RNA per sample. Total DNA/RNA was extracted using TRIzol Reagent as an alternative extraction method for DNA and RNA.

ATP Measurement

Analysis of total ATP levels was performed using a commercially available kit (ATPlite, PerkinElmer).

Oxygen Consumption

Cells were seeded at 30,000 cells per well on Seahorse XF24 tissue culture plates (Seahorse Bioscience Europe). The oxygen consumption was measured over a period of 2 min. At any condition, 5 consecutive measurements of OCR are done. After OCR measurement at baseline conditions, oligomycin, a blocker of ATP synthase is injected at 12 μM (final concentration in the cell 1.2 μM) to assess OCR_{ATP}.

Detection of Glutathione Species, NADPH and dNTPs

Metabolites from ECs grown on a 6-well plate were extracted in 300 μL of a 50:30:20 (methanol: acetonitrile: 20 mM Tris, pH 9.3) extraction buffer. Extraction samples were then centrifuged for 5 min at 15,000 x G and the supernatant was transferred to LC-MS vials. Targeted measurements of GSSG, GSH, $NADP^+$, NADPH, dATP, dTTP and dCTP were performed using a Dionex UltiMate 3000 LC System (Thermo Scientific) coupled to a Q Exactive Orbitrap mass spectrometer (Thermo Scientific) operated in negative mode. Practically, 35 μL of sample was injected on a SeQuant ZIC/ pHILIC Polymeric column (Merck Millipore). The gradient started with 20% of solvent B (10 mM NH_4-acetate in MQH_2O, pH 9.3) and 80% solvent A (LC-MS grade acetonitrile) and remained at 20% B until 2 min post injection. Next, a linear gradient to 80% B was carried out until 29 min. At 38 min the gradient returned to 40% B followed by a decrease to 20% B at 42 min. The chromatography was stopped at 58 min. The flow was kept constant at 100 μL per min at the column was placed at 25°C throughout the analysis. The MS was operated both in targeted MS2 mode using a spray voltage of 3.5 kV, capillary temperature of 320°C, sheath gas at 10.0, auxiliary gas at 5.0. For the targeted MS2 mode, AGC was set at 2e5, maximum IT at 100 ms, a resolution of 17.500 and an isolation window of 1.2 m/z. Data collection was performed using *Xcalibur* software (Thermo Fisher Scientific).

Glucose Consumption

Cells were incubated for 24 hr in growth medium. To 20 μL of medium 80 μL of 100% methanol was added and kept for 3 hr at −80°C in order to precipitate proteins. Following a centrifugation at 20,000 x g for 10 min, the supernatant was dried using a vacuum centrifuge. To the dried fraction, 50 μL of hydroxylamine hydrochloride solution (20 mg/mL in pyridine) was added. The samples were heated at 90°C for 60 min, followed by the addition of 100 μL of propionic anhydride. After 30 min incubation at 60°C, the samples were again evaporated to dryness and dissolved in 100 μL of ethyl acetate and transferred into GC vials for GC-MS analysis. The injection volume was 1 μL and samples were injected using a 1:20 split ratio. GC oven temperature was held at 80°C for 1 min, increased to 280°C at 20°C per min, and held for 3 min. The mass spectrometer operated in SIM mode and glucose was determined from the fragment at m/z 370 ($C_{17}H_{24}O_8N_1$), which contains carbon atoms C1–C5 of glucose. Data collection was performed using *Xcalibur* software.

Energy Balance Assessment

Samples were collected in 300 μL cold (chilled on dry ice) 50:30:20 (methanol: acetonitrile: 20 mM Tris, pH 9.3) extraction buffer and 100 μL of the mixture was injected onto an Agilent 1260 HPLC equipped with a C18-Symmetry column (150 x 4.6 mm; 5 μm) (Waters), thermostatted at 22.5°C. Flow rate was kept constant at 1 mL/min. A linear gradient using solvent A (50 mM NaH_2PO_4, 4 mM tetrabutylammonium, adjusted to pH 5.0 using H_2SO_4) and solvent B (50 mM NaH_2PO_4, 4 mM tetrabutylammonium, 30% CH_3CN, adjusted to pH 5.0 using H_2SO_4) was accomplished as follows: 95% A for 2 min, from 2 to 25 min linear increase to 100% B, from 25 to 27 min isocratic at 100% B, from 27 to 29 min linear gradient to 95% A and finally from 29 to 35 min at 95% A. Detection of ATP, ADP and AMP occurred at 259 nm. The energy charge was calculated using the following equation:

$$\text{Energy charge} = \frac{[\text{ATP}] + \frac{1}{2}[\text{ADP}]}{[\text{ATP}] + [\text{ADP}] + [\text{AMP}]}$$

^{13}C Tracer Experiments and Metabolite Levels

For ^{13}C-carbon incorporation from palmitate in metabolites, cells were incubated for 48 hr with labeled substrates. For ECs, [U-^{13}C] palmitate, [U-^{13}C]glucose, [U-^{13}C]glutamine, [U-^{13}C]acetate labeling was done in the setting of 100% labeling, whereby all cold metabolites in growth medium were replaced by 100 μM [U-^{13}C]palmitate, 5.5 mM [U-^{13}C]glucose, 2 mM [U-^{13}C]glutamine (Cambridge isotope laboratories) or 500 μM [U-^{13}C]acetate (Sigma-Aldrich) respectively. For palmitate labelling charcoal stripped serum (which does not contain any fatty acids) was used in growth medium (Sigma-Aldrich). Metabolites for the subsequent mass spectrometry analysis were prepared by quenching the cells in liquid nitrogen followed by a cold two-phase methanol-water-chloroform extraction (Schoors et al., 2015). Phase separation was achieved by centrifugation at 4°C and the methanol-water phase containing polar metabolites was separated and dried using a vacuum concentrator. The dried metabolite samples were stored at −80°C (Schoors et al., 2015). Polar metabolites were derivatized for 90 min at 37°C with 7.5 μL of 20 mg/mL methoxyamine in pyridine and subsequently for 60 min at 60°C with 15 μL of N-(tert-butyldimethylsilyl)-N-methyl-trifluoroacetamide, with 1% tert-butyldimethyl-chlorosilane (Schoors et al., 2015). Isotopomer distributions and metabolite levels were measured with a 7890A GC system (Agilent Technologies) combined with a 5975C Inert MS system (Agilent Technologies). One microliter of sample was injected onto a DB35MS column in splitless mode using an inlet temperature of 270°C (Schoors et al., 2015). The carrier gas was helium with a flow rate of 1 mL per min. Upon injection, the GC oven was held at 100°C for 3 min and then ramped to 300°C with a gradient of 2.5°C per min. The MS system was operated under electron impact ionization at 70 eV and a mass range of 100–650 amu was scanned. Isotopomer distributions were extracted from the raw ion chromatograms using a custom Matlab M-file, which applies consistent integration bounds and baseline correction to each ion. In addition, we corrected for naturally occurring isotopes using the method of Fernandez et al. (Fernandez et al., 1996). For relative metabolite levels, the total ion count was normalized to the internal standards norvaline and glutarate and to the protein content. To correct for enrichment dilution, we used previously reported methods, i.e. we divided the

fractional contribution of a labeled metabolite of interest by the fractional contribution of its precursor. The total contribution of carbon was calculated using the following equation:

$$\text{Total contribution of carbon} = \sum_{i=0}^{n} i * m_i \Big/ \left(n * \sum_{i=0}^{n} m_i \right)$$

Herewith, "n" is the number of C atoms in the metabolite, "i" represents the different mass isotopomers and "m" refers to the abundance of a certain mass. Glycolytic carbon contribution was calculated based on [U-^{13}C]glucose labeling and label dilution in pyruvate . For total metabolite levels, arbitrary units of the metabolite of interest were normalized to the protein content.

PC-dependent anaplerosis was estimated from the difference of m+3 malate and m+3 succinate using [U-^{13}C]glucose, as described previously (Christen et al., 2016). Briefly, malate m+3 from [U-^{13}C]glucose is generated by PC flux, but can also arise from an oxidative TCA cycle flux. Succinate m+3 from [U-^{13}C]glucose can arise from an oxidative TCA cycle flux, but not from PC flux (given that reverse succinate dehydrogenase flux is marginal or not present). Thus, under the prerequisite that pyruvate enrichment from [U-^{13}C]glucose is similar, comparing malate m+3 and succinate m+3 allows to conclude about relative changes of PC-dependent anaplerosis.

In Vitro Functional Assays

Proliferation

EC Proliferation was quantified by incubating cells for 2 hr with 1 μCi/mL [6-^{3}H]thymidine (Perkin Elmer). Thereafter, cells were fixed with 100% ethanol for 15 min at 4°C, precipitated with 10% TCA and lysed with 0.1 N NaOH. The amount of [6-^{3}H]-thymidine incorporated into DNA was measured by scintillation counting.

LDH Viability Assay

Cell survival was assessed by lactate dehydrogenase (LDH) release into the media using the LDH assay kit (Roche) as indicated in manufacturer's specifications, whereby low LDH release signifies low cell death and high survival. 1.2 μM oligomycin (Sigma-Aldrich) was used to verify whether pharmacological targeting of ATP can affect viability of ECs upon induction of quiescence and or CPT1A^{KD}.

Trans-endothelial Electrical Resistance

25,000 ECs were seeded in growth medium on 6.5 mm 0.1% gelatin-coated polyester transwells, 0.4 μm pore size (Costar ref. 3470, Sigma-Aldrich). The trans-endothelial electrical resistance (TEER) was measured using the Endohm-6 electrode (World Precisions Instruments) connected to an EVOM2 voltohmmeter (World Precisions Instruments). Gelatin-coated wells without cells were used to measure the intrinsic electrical resistance of the inserts and these values were then subtracted to the values measured in the presence of cells. Measurements were performed every day, taking at least 2 measurements per treatment. Overnight incubation with etomoxir (100 μM) and trimetazidine (TMZ) (250 μM; Sigma-Aldrich) was used to assess the effect of pharmacological FAO inhibition, LPS (1 μg/mL) (*Escherichia coli*, 0111:B4, Sigma-Aldrich) was used to assess the effect of the stressors, hydroxycitrate (HCA) (1mM; Sigma-Aldrich) was used to assess the inhibition of ATP-dependent citrate lyase. The mitochondrial ROS scavenger mitoTEMPO (Sigma-Aldrich) was used with a concentration of 5 μM.

Leukocyte Adhesion Assay

Whole blood from healthy human volunteers was collected (with approval from the Medical Ethical Committee KU Leuven/UZ Leuven and informed consent obtained from all subjects) and anticoagulated with K_2EDTA (1.8 mg/mL, using plastic whole blood spray-coated K_2EDTA tubes, Bection Dickinson). Peripheral blood mononuclear cell (PBMC) were isolated by gradient centrifugation over Ficoll-paque plus (GE healthcare). PBMCs were labelled with Calcein (cell-permeant dye, Thermo Fisher Scientific). HUVECS (plated 7 days before (7.5 x 10^4 cells/well, 12-wells plate), were washed with PBS and incubated either with vehicle (sterile PBS), etomoxir (100 μM) or LPS (1 μg/mL) overnight (37°C, 5% CO_2). After this period, medium was removed and ECs were washed with PBS. The mononuclear cells were added (5 x 10^5/well) and incubated for 60 min (37°C, 5% CO_2). Non-adherent cells were removed by washing 5 times with PBS and cells where fixed using 4% PFA. Five fields per well, randomly chosen, were analyzed, and the number of adherent leukocytes per field was determined using a Leica DMI6000B microscope (magnification 20X).

Analysis of ROS Species

Intracellular ROS Analysis

Intracellular ROS levels were measured using 5-(and-6)-chloromethyl-2′,7′-dichlorodihydrofluorescein diacetate, acetyl ester (CM-H_2DCFDA) according to the manufacturer's instructions (Thermo Fisher Scientific). CM-H_2DCFDA is metabolized by intracellular esterases to a non-fluorescent molecule, which is oxidized by H_2O_2 to the fluorescence product CM-DCF. The intracellular ROS levels were determined by pre-incubation of the ECs for 30 min with 10 μM CM-H_2DCFDA and H_2O_2 scavenging capacity was determined after a subsequent incubation for 0-2 hr with 50 μM H_2O_2 (Merck, Milipore) in serum free M199. The mitochondrial ROS scavenger mitoTEMPO (Sigma-Aldrich) was used with a concentration of 5 μM. The fluorescent intensity was measured according to the manufacturer's instructions.

Mitochondrial ROS Analysis via MitoSOX

Intracellular accumulation of superoxide was estimated using MitoSOX Red (Thermo Fisher Scientific), which is selectively targeted to the mitochondria, where it is oxidized by superoxide and exhibits red fluorescence upon binding to nucleic acids. Cells were

loaded with MitoSOX at 2.5 μM for 30 min, collected by trypsinization and washed with PBS supplemented with 2% FBS. Using a flow cytometer, MitoSOX Red was excited at 488 nm and fluorescence emission at 575 nm was measured. Fluorescence intensity was used as measurement of mitochondrial superoxide production and the data were analyzed with the FlowJo 8.8.6 software.

Total Levels of H_2O_2

Total levels of H_2O_2 were measured by using the Amplex Red Hydrogen Peroxide/Peroxidase Assay Kit (Thermo Fisher Scientific), according to the manufacturer's instructions.

Mitochondrial Levels of H_2O_2

Measurements of the mitochondrial levels of H_2O_2 were performed using the HyPER-dMito probe (Evrogen) as previously described (Belousov et al., 2006). Briefly, ECs were transduced overnight with HyPER-dMito (cloned in the pRRLsinPPT.CMV.MCS MM W prevector) and re-fed with fresh medium the next day. Transduced cells were used for confocal imaging using a Zeiss LSM 780 confocal microscope (oil objective: x40) (Carl Zeiss) and were treated with or without 50 μM H_2O_2 for 10 min. Cells were placed in the microscope stage incubator and HyPER-dMito fluorescence was activated by 488 nm or 405 nm laser. Band pass 530/40 emission filter was used in both cases. For each condition 10 independent images were taken. To assess mitochondrial levels of H_2O_2, the ratio of fluorescence intensity upon excitation at 488nm over fluorescence intensity upon excitation at 405 nm (ratio 488/405 nm) was calculated.

OH° Detection by Electron Paramagnetic Resonance (EPR) Spectroscopy

Quiescent (QEC) or proliferating cells (PEC) were washed twice with PBS and incubated for 3-5 min with trypsin/EDTA at 37°C. Harvested cells were centrifuged for 5 min at 1,200 rpm, washed with DPBS, and resuspended in PBS at a concentration of $2x10^6$ cells/mL. Spin trapping reagents 5-diisopropoxyphosphoryl-5-methyl-1-pyrroline N-oxide (DIPPMO, final concentration 50 mM) (Enzo Life Science) and diethylenetriaminepentaacetic acid (DTPA, final concentration 1 mM) (Sigma-Aldrich) were added and the solution was transferred to a flat quartz cell for the EPR measurements. This ensured reproducible measurement as the whole resonator was filled with the same volume of material. For measurement on lysates, cells were lysed by sonication (20 s, Labsonic U, B. Braun). For control experiments with superoxide dismutase-polyethylene glycol (SOD-PEG, final concentration 200 U/mL) (Sigma-Aldrich) or catalase-peg (CAT-PEG, final concentration 100 U/mL) (Sigma-Aldrich), cells were preincubated for 30 min (37°C) with the appropriate enzyme before adding the spin trap reagents. EPR measurements were performed using a Bruker EMX-Plus spectrometer (Bruker, Rheinstetten, Germany), operating in X-band (9.85 GHz) and equipped with a SHQ high- sensitivity resonator. Settings used were as follows: microwave power: 20 mW; modulation frequency: 100 kHz; modulation amplitude: 0.1 mT (lysate) or 0.2 mT (cells); receiver gain: 60 dB; time constant: 10.24 ms; conversion time, 50.04 ms; data points, 1024; sweep width, 20 mT; number of scan: 15. Computer simulations were performed using Winsim from the Public Electron Paramagnetic Resonance Software Tools library of the NIH (USA).

Immunochemistry and Morphometry

Quantification of VE-cadherin Junctions

Cells were fixed with 4% PFA for 10 min at room temperature and subjected to immunofluorescence staining for adherence junctions using anti-VE-cadherin (Thermo Fisher Scientific) and Alexa-488 Fluor conjugated phalloidin (Thermo Fisher Scientific). Alexa-568 or -647 conjugated secondary antibodies were used (Thermo Fisher Scientific). Imaging was performed using a Zeiss LSM 780 confocal microscope (oil objectives: x40 NA 1.3, x63 NA 1.4, x100 NA 1.46) (Carl Zeiss). Junctional length was calculated by measuring the length of all segments of continuous and discontinuous junctions on confluent ECs stained for VE-cadherin as described (Cantelmo et al., 2016). The sum of all segments was considered the total junctional length (100%), and the sum of all discontinuous segments was calculated as the percentage of total junctional length. A minimum of 5 fields was quantified (≈30 cells per field) per experiment.

β-galactosidase Senescence Staining

Staining was performed as previously described (Debacq-Chainiaux et al., 2009). Briefly, The EC cultures were fixed for 5 min at room temperature with fixation solution (2% formaldehyde (vol/vol) and 0.2% glutaraldehyde (vol/vol) in PBS) followed by overnight incubation with the staining solution (40 mM citric acid/Na phosphate buffer, 5 mM $K_4[Fe(CN)_6]$, 5 mM $K_3[Fe(CN)_6]$, 150 mM sodium chloride, 2 mM magnesium chloride) and 1 mg/mL X-gal (Thermo Fisher Scientific) in distilled H_2O. Cells were rinsed twice with PBS and once with 100% methanol. The stained cell culture plates were protected from the light and air-dried. The β-galactosidase staining was imaged using phase-contrast microscopy.

PCR Chromatin Immunoprecipitation

Cultured cells, treated or not with the Notch inhibitor N-[N-(3,5-difluorophenacetyl)-L-alanyl]-S-phenylglycine t-butyl ester (DAPT; 10 μM) (Sigma-Aldrich) overnight, were fixed with 1% formaldehyde (16% formaldehyde (w/v), Methanol-free, Thermo Fisher Scientific) for 8 min. Glycine (125 μM) was added for 5 min. Cells were washed twice with ice-cold PBS 0.5% Triton-X100, scraped and collected by centrifugation (1,000 × g for 5 min at 4°C). The pellet was resuspended in 1,400 μL of modified RIPA buffer (50 mM Tris-HCl pH 8, 150 mM NaCl, 2 mM EDTA pH 8, 1% Triton-X100, 0.5% Sodium deoxycholate, 1% SDS, 1% protease inhibitors). The lysate was sonicated for 4 min by using a 250 Digital Sonifier (Branson) with 0.7 s 'On' and 1.3 s 'Off' pulses at 40% power amplitude, yielding a DNA fragments between 100 and 1,000 bp. The lysate was centrifuged for 10 min at 16,000 × g (4°C), and supernatant transferred to a new eppendorf tube. 50 μL of sheared chromatin was set apart as "input", and 5 μg of either rat anti-Notch1 (Cell Signaling Technology) or mouse anti-V5 tag (Thermo Fisher Scientific) were added to the remainder of the chromatin. Samples

were incubated overnight at 4°C on a rotator. 20 μL Pierce Protein A/G Magnetic Beads (Thermo Fisher Scientific) were added to the samples and incubated at 4°C for at least 5 hr. A/G Magnetic Beads were collected and washed 5 times with washing buffer (50 mM Tris-HCl, 200 mM LiCl, 2 mM EDTA, pH 8, 1% Triton, 0.5% Sodium deoxycholate, 0.1% SDS, 1% protease inhibitors), and twice with TE buffer. The A/G magnetic beads were resuspended in 50 μL of TE buffer, and 1.5 μL of RNase A (Thermo Fisher Scientific) was added to the A/G beads samples and to the input, followed by incubation for 30 min at 37°C. After addition of 1.5 μL of proteinase K (Thermo Fisher Scientific) and overnight incubation at 65°C in a thermoshaker (800 rpm), the DNA was purified using 1.8 × volume of Agencourt AMPure XP (Beckman Coulter) according to the manufacturer's specifications, and eluted in 20 μL of TE buffer (Thermo Fisher Scientific). The input, control IgG and immunoprecipitated DNA fractions were then subjected to quantitative PCR using SYBR Green (PowerUp SYBR Green, Thermo Fisher Scientific). Primer sequences are listed in the Key Resources Table. Raw Ct values were analyzed and results were presented as % of input.

Luciferase Reporter Assay

Sequences verified by PCR were cloned into the pGL3 basic luciferase plasmid (Promega) lacking promoter and enhancer elements. HUVECs were transduced with control lentiviruses or $NICD^{OE}$ lentiviruses. Four days after viral transduction, cells were trypsinized and transfected with empty pGL3 plasmids or plasmids containing sequences of the *CPT1A* promoter, as identified by chromatin immunoprecipitation (ChIP)-qPCR, using Nucleofector transfection reagent (Lonza), as per manufacturer's specifications. Cells were co-transfected with the respective luciferase reporters and also the Renilla plasmid, as a control, and allowed to grow for 72 hr before being collected with PBS, centrifuged, then lysed. Luciferase activity was measured by Dual Luciferase Reporter Kit (Promega) according to the manufacturer's specifications.

Mouse Studies

In Situ Detection of ECs Superoxide Levels

Aortas and portal veins were harvested from the animals at 4 or 12 hr after LPS injection (10 mg/kg, i.p.) and treated i.p. with 400 μL vehicle or 0.5 M sodium acetate (Sigma-Aldrich) solution daily, were opened longitudinally for en-face dehydroethidium (DHE; Thermo Fisher Scientific) staining. DHE (20 μmol/L) was topically applied to the samples and incubated in a light-protected humidified chamber at 37°C for 30 min followed by Hoechst33342 (1 μg/mL; Thermo Fisher Scientific) staining for 15 min and finally Alexa-647 conjugated isolectin B4 (Thermo Fisher Scientific) for 1 hr. Imaging was performed immediately using a Zeiss LSM 780 confocal microscope (oil objective: x40 NA 1.3) (Carl Zeiss). The endothelium was identified by an isolectin B4 positive signal. For all images in a single experiment, the samples were all stained at the same time, and acquisition settings were kept constant for all image acquisitions. Quantification of DHE fluorescence intensity was performed using Fiji software. Average intensity images were generated and ECs nuclei were selected using the particle-analyzer tool. Per sample, 5 images were analyzed and corrected total cell fluorescence was calculated for DHE.

Determination of Cytokine Concentrations

Levels of cytokines were measured in blood serum of LPS treated $CPT1A^{\Delta EC}$ mice and their WT littermates using MACSPlex Cytokine Kit according to the manufacturer's instructions (mouse, Miltenyi Biotec).

Leukocyte Infiltration into the Lungs

Lungs were dissected and fixed in 4% PFA overnight at 4°C, dehydrated, embedded in paraffin and sectioned. Immunostaining of leukocytes was done with rat anti-Mouse CD45 antibody (BD Pharmingen). The sections were then incubated with an appropriate secondary antibody (Jackson Immuno Research) and TSA Cy3 amplification (Perkin Elmer). Nuclei were counterstained with Hoechst33342. Imaging was performed using a Leica DMI6000B inverted microscope (Leica Microsystems). Morphometric analysis of the $CD45^+$ area in % of lung area was done using Leica MM AF powered by MetaMorph analysis software.

DSS-induced Acute Colitis Model

$CPT1A^{\Delta EC}$ and WT mice were exposed to vehicle or 2.5% dextrane sulfate sodium (DSS) (36,000-50,000 M.Wt., MP Biomedicals) in their drinking water for 7 consecutive days. The severity of colitis was evaluated by assessing the disease activity index (DAI) (which scores body weight loss, stool consistency, and blood in the stool and anal region) of $CPT1A^{\Delta EC}$ and WT mice under DSS treatment. On day 7, mice were injected via the tail vein with dextran-rhodamine (70,000 kDA, Thermo Fisher Scientific). Ten min after injection, mice were perfused and fixed (using 1% PFA perfusion) and the colon was harvested and processed for immunohistochemistry. Colon sections were stained with H&E for morphological analyses, with anti-CD105 (R&D Systems) to identify blood vessels, anti-CD45 antibodies to analyze immune cell infiltration and PCNA to identify proliferating cells. The sections were then incubated with an appropriate secondary antibody (Jackson Immuno Research) and TSA Fluorescein or TSA Cy5 amplification (Perkin Elmer) when needed. Nuclei were counterstained with Hoechst33342 (Thermo Fisher Scientific). Imaging was performed using a Leica DMI6000B inverted microscope (Leica Microsystems). The leakiness of the vessels was measured by quantifying the extravascular dextran-rhodamine positive area. Morphometric analysis of the $CD45^+$ area in % of colon area was done using Leica MM AF powered by MetaMorph analysis software. Quantification of the vessel area in the colonic mucosa was done using Fiji software. EC proliferation was measured as the number of $PCNA^+$ $CD105^+$ ECs and expressed as a percentage of the total number of $CD105^+$ ECs per imaged filed using Fiji software.

Human Tissue Analysis

In Situ Detection of CPT1A in the Vasculature

Human lung and kidney sections, obtained from Pathology Department from University of Leuven (KU Leuven), were used for immunostaining with anti-CD31 (Dako) and anti-CPT1A (Proteintech) primary antibodies. Appropriate fluorescently conjugated secondary antibodies (Jackson Immuno Research) were used, followed by TSA Cy5 amplification (Perkin Elmer) when needed. Imaging was performed immediately using a Zeiss LSM 780 confocal microscope (oil objective: x40) (Carl Zeiss).

QUANTIFICATION AND STATISTICAL ANALYSIS

Data represent mean ± SEM of at least three independent experiments. Statistical significance was calculated by standard two-tailed t test with Welch's correction, ANOVA (for multiple comparisons within one dataset), one sample t test (for comparisons to point-normalized data) and by log-rank test (for comparisons of survival distributions of two groups) using Prism v6.0f. When inter-experimental variability was large between experiments with ECs isolated from individual umbilical cord donors, mixed model statistics (R version 3.2.4 using Kenward-Roger approximation) was used with experiment (i.e. donor) as random factor to correct for confounding variation between individual EC isolations. Self-contained gene set analysis was performed via rotation gene set analysis (R, limma package). $P < 0.05$ was considered statistically significant.

DATA AND SOFTWARE AVAILABILITY

Data Resources

The microarray data have been deposited in the GEO database under accession number GEO: GSE89174. The RNA sequencing data have been deposited in the Array Express under accession number Array Express: E-MTAB-6595.

Software

All software is freely or commercially available and is listed in the STAR Methods description and Key Resources Table.